Geophysical Journal International

Geophys. J. Int. (2023) **233,** 641–662 https://doi.org/10.1093/gji/ggac473
Advance Access publication 2022 November 30
GJI Seismology

The 2015–2017 Pamir earthquake sequence: foreshocks, main shocks and aftershocks, seismotectonics, fault interaction and fluid processes

Wasja Bloch,[1,2] Sabrina Metzger,[1] Bernd Schurr,[1] Xiaohui Yuan,[1] Lothar Ratschbacher,[3] Sanaa Reuter,[3] Qiang Xu,[4,5] Junmeng Zhao,[4,5] Shokhruhk Murodkulov[6] and Ilhomjon Oimuhammadzoda[7]

[1] *GFZ German Research Centre for Geosciences,* 14473 *Potsdam, Germany. E-mail: wbloch@eoas.ubc.ca*
[2] *Department of Earth, Ocean and Atmospheric Sciences, University of British Columbia, Vancouver V6T 1Z4, Canada*
[3] *Geologie, Technische Universität Bergakademie Freiberg,* 09599 *Freiberg, Germany*
[4] *Key Laboratory of Continental Collision and Plateau Uplift, Institute of Tibetan Plateau Research, Chinese Academy of Sciences, Beijing* 100101*, China*
[5] *CAS Center for Excellence in Tibetan Plateau Earth Sciences, Beijing* 100101*, China*
[6] *Institute of Geology, Earthquake Engineering and Seismology, National Academy of Sciences, Dushanbe, Tajikistan*
[7] *Department of Geology under the Government of the Republic of Tajikistan, Dushanbe, Tajikistan*

Accepted 2022 November 28. Received 2022 November 18; in original form 2022 June 27

SUMMARY

A sequence of three strong (M_W 7.2, 6.4, 6.6) earthquakes struck the Pamir of Central Asia in 2015–2017. With a local seismic network, we recorded the succession of the foreshock, main shock and aftershock sequences at local distances with good azimuthal coverage. We located 11 784 seismic events and determined 33 earthquake moment tensors. The seismicity delineates the tectonic structures of the Pamir in unprecedented detail, that is the thrusts that absorb shortening along the Pamir's thrust front, and the strike-slip and normal faults that dissect the Pamir Plateau into a westward extruding block and a northward advancing block. Ruptures on the kinematically dissimilar faults were activated subsequently from the initial M_W 7.2 Sarez event at times and distances that follow a diffusion equation. All main shock areas but the initial one exhibited foreshock activity, which was not modulated by the occurrence of the earlier earthquakes. Modelling of the static Coulomb stress changes indicates that aftershock triggering occurred over distances of ≤90 km on favourably oriented faults. The third event in the sequence, the M_W 6.6 Muji earthquake, ruptured despite its repeated stabilization through stress transfer in the order of –10 kPa. To explain the accumulation of $M_W > 6$ earthquakes, we reason that the initial main shock may have increased nearby fault permeability, and facilitated fluid migration into the mature fault zones, eventually triggering the later large earthquakes.

Key words: Asia; Earthquake interaction, forecasting and prediction; Seismicity and tectonics; Continental neotectonics; Dynamics: seismotectonics; Dynamics and mechanics of faulting.

1 INTRODUCTION

The Pamir occupies the northwestern tip of the India–Asia collision zone, where several major mountain belts—the Tian Shan, Kunlun Shan, Karakorum and Hindu Kush—and two large depressions—the Tarim and Afghan-Tajik basins—converge (Fig. 1). It exhibits some of the highest strain rates for an intracontinental setting, both within the broad India–Asia collision zone and globally (Kreemer *et al*. 2014). Deformation involves shortening and dextral strike-slip shear along its northern margin and sinistral strike-slip faulting and extension in its interior, the Pamir Plateau (Schurr *et al*. 2014).

On 7 December 2015, the moment magnitude M_W 7.2 Sarez sinistral strike-slip earthquake hit the Pamir interior. It ruptured three segments of the ∼NNE-striking Sarez-Karakul Fault System (SKFS) with a total length of ∼80 km (Fig. 1a; Metzger *et al*. 2017; Sangha *et al*. 2017; Elliott *et al*. 2020). In the aftermath two $M_W > 6.4$ and multiple $M_W > 5$ earthquakes occurred on various segments of the nearby fault networks. Specifically, the June 26, 2016 M_W6.4 Sary-Tash earthquake ruptured an ∼E-striking reverse fault below the Main Pamir Thrust System (MPTS; He *et al*. 2018), ∼90 km NNE of the northern end of the Sarez rupture, and the November 25, 2016 M_W6.6 Muji earthquake broke two

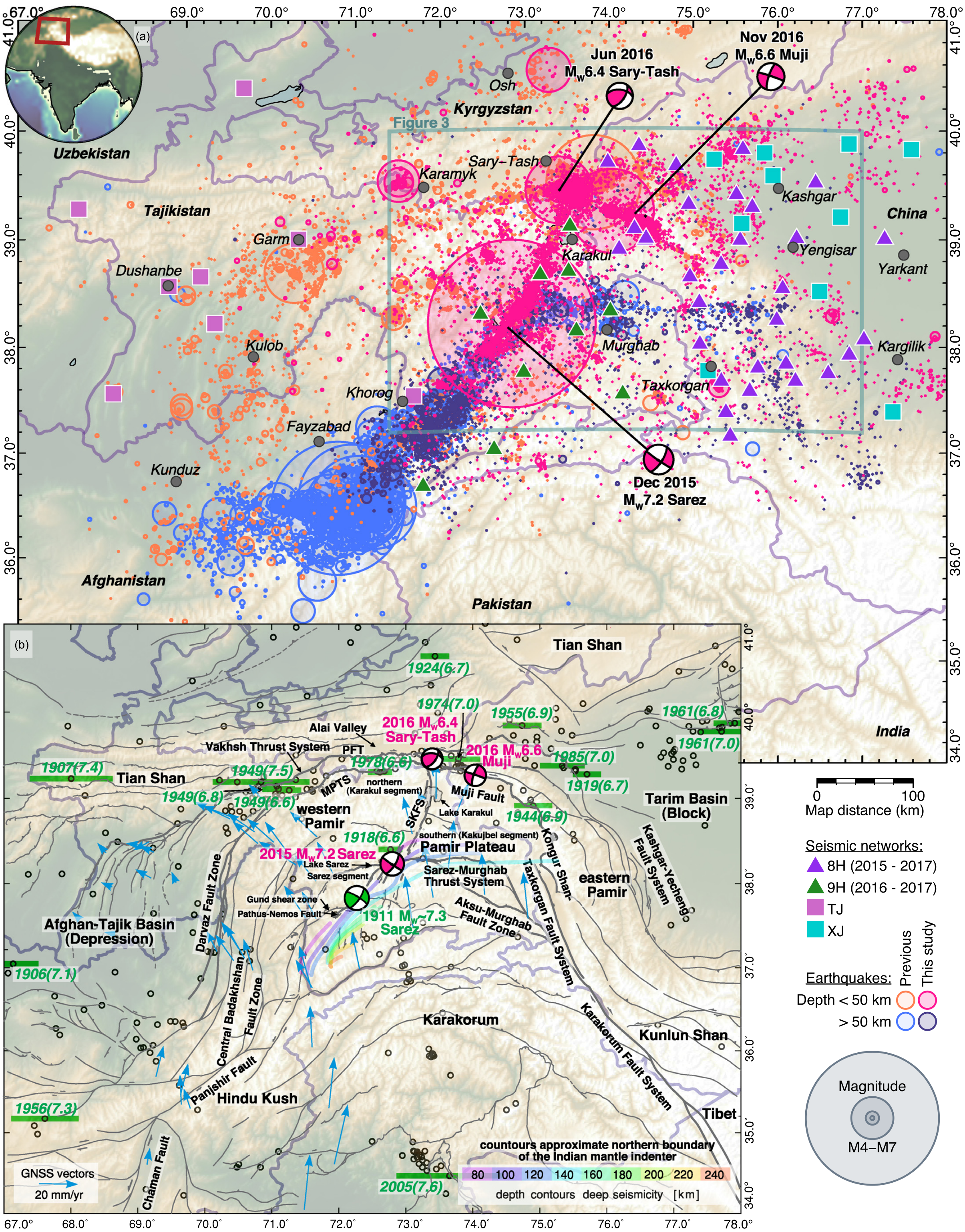

Figure 1. (a) Location of the study area, seismic stations, seismicity from this and previous (Schurr *et al*. 2014; Kufner *et al*. 2017, 2018) studies, and moment tensors of the three largest earthquakes of the sequence. Crustal seismicity (depth < 50 km) delineates the active fault zones. Intermediate depth seismicity (depth > 50 km) indicates subduction of Indian lithosphere beneath the Hindu Kush (Kufner *et al*. 2017, 2021) and delamination of Asian lithosphere beneath the Pamir (Sippl *et al*. 2013b; Bloch *et al*. 2021). (b) Cenozoic fault map with the neotectonic faults discussed in the text highlighted and named. Instrumentally recorded earthquakes since 1900 with $M > 5.5$ as black circles and $M > 6.5$ as green bars (Bondár *et al*. 2015; Di Giacomo *et al*. 2018; ISC 2021) indicating approximate rupture length (Wells & Coppersmith 1994). Focal mechanism of the 1911 Sarez earthquake is from Kulikova *et al*. (2016) and its location follows Elliott *et al*. (2020). Depth contours of intermediate-depth seismicity are from Schurr *et al*. (2014). Global Navigation Satellite System (GNSS) displacement rates from the Pamir Plateau and its western foreland are from Perry *et al*. (2019). MPTS, Main Pamir Thrust System. PFT, Pamir Frontal Thrust. SKFS, Sarez-Karakul Fault System.

segments of the ∼WNW-striking Muji Fault (Bie *et al*. 2018; Li *et al*. 2018, 2019), a dextral strike-slip fault ∼30 km SW of the Sary-Tash earthquake (Fig. 1a). Even for a region as seismically-active as the Pamir, this sequence was unusual: long-term earthquake bulletins (e.g. the Global Earthquake Model ISC-GEM; Di Giacomo *et al*. 2018; ISC 2021) report only 18 $M_W > 6.5$ earthquakes in the region between 1900 and 2015 (Fig. 1b). The probability that the three recent $M_W > 6.4$ earthquakes occurred independently of each other, i.e. following a Poisson process, is 0.05 per cent. Furthermore, the subsequent earthquakes showed a conspicuous activation pattern, with earthquakes occurring at increasing distances from the initial main shock, on kinematically dissimilar fault zones, and over comparatively large distances (Video 1)

Earthquakes often occur in spatio-temporal clusters. Examples in the central Apennines, Italy (e.g. Chiaraluce *et al*. 2003; Valoroso *et al*. 2013; Chiaraluce *et al*. 2017; Michele *et al*. 2020), Southern California, United States of America (e.g. Hauksson *et al*. 1993; Parsons & Dreger 2000; Freed & Lin 2001; Toda & Stein 2020; Chen *et al*. 2020), Baluchistan, Pakistan (Yadav *et al*. 2012), the South Iceland Seismic Zone (e.g. Einarsson *et al*. 1981; Árnadóttir *et al*. 2003; Hreinsdóttir *et al*. 2009) or the Sunda Arc, Indonesia (e.g. Briggs *et al*. 2006; Pollitz *et al*. 2006; Wiseman & Burgmann 2011) demonstrate how sequences of earthquakes may unfold over time. Attempts to foresee the imminent occurrence of larger events during periods of seismic unrest encompass the estimation of elastic or viscoelastic Coulomb failure stress changes on adjacent fault segments (e.g. Toda *et al*. 1998; Stein 1999; Nalbant *et al*. 2005; Lorenzo-Martín *et al*. 2006; Wiseman & Burgmann 2011; Ryder *et al*. 2012; Toda & Stein 2020; Chen *et al*. 2020), and the detection of foreshock cascades (e.g. Ellsworth & Bulut 2018; Chen *et al*. 2020; Schurr *et al*. 2020). Sometimes, fluids escape from an activated fault network and induce fault slip (Hamling & Upton 2018), but unambiguous identification of large earthquakes being triggered by increased fluid pressure is restricted to controlled injection experiments (e.g. Ellsworth *et al*. 2019; Woo *et al*. 2019). In any case, investigations of fault interactions in earthquake sequences require intimate knowledge about the structure of the involved fault segments (e.g. Mildon *et al*. 2019).

Since August 2015, we had a temporary seismic network in operation in the eastern Pamir in the Xinjiang province of China. It recorded the initial December 2015 Sarez earthquake (Fig. 1a). In February 2016, we deployed a network on the Pamir Plateau of Tajikistan in the vicinity of the Sarez earthquake rupture. The combined networks recorded then both the June 2016 Sary-Tash and the November 2016 Muji earthquake sequences with a very good azimuthal coverage. Additional moderate earthquakes with their own fore- and aftershock sequences augmented the seismotectonic record.

After introducing the neotectonic framework (Section 2), the dataset, and the methodology (Section 3), we document the spatio-temporal foreshock, main shock and aftershock patterns (Section 4). We then use the obtained moment tensors and precise seismic event locations to determine the location, orientation, kinematics, and activation times of the seismically active structures in the Pamir and southern Tian Shan region, associate them with geologically mapped faults, and evaluate their seismic history. To identify long-term seismicity patterns, we compare our findings with the results of an earlier experiment (Section 5; Sippl *et al*. 2013b; Schurr *et al*. 2014). We construct a Coulomb stress-transfer model that honours the spatio-temporal seismic activation patterns and aseismic displacements inferred from interferometric synthetic-aperture radar (InSAR) to investigate processes of earthquake interaction and nucleation (Section 6). The combined results allow us to reason about the possible involvement of coseismically mobilized fluids in fault activation (Section 7).

2 NEOTECTONIC FRAMEWORK

In the Pamir, northward displacement at rates of 13–19 mm/yr is currently accommodated along its margins by (i) crustal shortening along the MPTS—which yielded the June 2016 earthquake—in the north, in particular the Pamir Frontal Thrust, (ii) the sinistral Darvaz Fault Zone in the west and northwest, (iii) the dextral Karakorum Fault System in the southeast and (iv) the Kongur Shan-Taxkorgan Normal Fault System in the Chinese eastern Pamir (Fig. 1; e.g. Jade *et al*. 2004; Zubovich *et al*. 2010; Ischuk *et al*. 2013; Schurr *et al*. 2014; Chevalier *et al*. 2015; Zubovich *et al*. 2016; Metzger *et al*. 2020; Zubovich *et al*. 2022). The Karakorum Fault System probably links with the Sarez-Murghab Thrust System via the Aksu-Murghab Fault Zone on the Pamir Plateau (Robinson 2009; Rutte *et al*. 2017). The dextral transpressive Kashgar-Yecheng Fault System (Cowgill 2009) linked shortening in the western Kunlun Shan with that along the MPTS; since ∼5 Ma (Sobel *et al*. 2011) and up to now (Zubovich *et al*. 2010), the Pamir and the Tarim basin have been moving north at about the same rate, rendering the transform component mostly inactive. The Muji Fault—that yielded the November 2016 earthquake—links ∼E–W extension along the Kongur Shan Normal Fault System to the MPTS (Schurr *et al*. 2014; Sippl *et al*. 2014; Li *et al*. 2019). The Kongur Shan Normal Fault System has accommodated ≥35 km of ∼E–W extension, mostly since ∼7 Ma (Robinson *et al*. 2004, 2007; Thiede *et al*. 2013); extension and dextral strike-slip along the Muji Fault are ongoing, as implied by seismicity and the divergence of the Global Navigation Satellite System (GNSS) velocity field between Pamir's interior and the Tarim block (Zubovich *et al*. 2010; Li *et al*. 2019).

In the interior of the Pamir, the active displacement field is composed of bulk northward movement combined with ∼E–W extension (Ischuk *et al*. 2013; Zhou *et al*. 2016). The crust hosts sinistral strike-slip faulting on ∼NE-striking planes, dextral strike-slip faulting on conjugate planes, and—to a lesser degree—normal faulting on ∼N-striking planes (Schurr *et al*. 2014). In the interior of the eastern Pamir the lack of significant seismicity demonstrates that it is moving northward en bloc; this agrees with the GNSS data. The only ∼NE-striking sinistral-transtensive fault system of the Pamir interior, which has a clear morphologic expression and is seismically active, is the SKFS, which yielded the initial December 2015 earthquake. It stretches from south of Lake Sarez to north of Lake Karakul (Strecker *et al*. 1995; Schurr *et al*. 2014; Metzger *et al*. 2017; Elliott *et al*. 2020). The northern SKFS is interpreted as a horst-graben structure (Nöth 1932; Strecker *et al*. 1995), the southern SKFS currently shows dominant sinistral strike-slip and subordinate normal displacements (Metzger *et al*. 2017; Elliott *et al*. 2020). Its southward continuation is the proposed source structure of an $M_W \sim 7.3$ earthquake that hit the Pamir in 1911 (Fig. 1b; Kulikova *et al*. 2016; Elliott *et al*. 2020). The ∼E–W extension—increasing into the western Pamir—is driven by westward gravitational collapse of thickened Pamir-Plateau crust into the Tajik Depression (Stübner *et al*. 2013; Schurr *et al*. 2014; Metzger *et al*. 2020).

Beneath the Pamir, Asian lithosphere forms a ∼90° arc that is retreating northward and westward as traced by intermediate-depth seismicity (60–300 km; Schneider *et al*. 2013; Sippl *et al*. 2013a). Kufner *et al*. (2016) and Bloch *et al*. (2021) inferred that the Asian

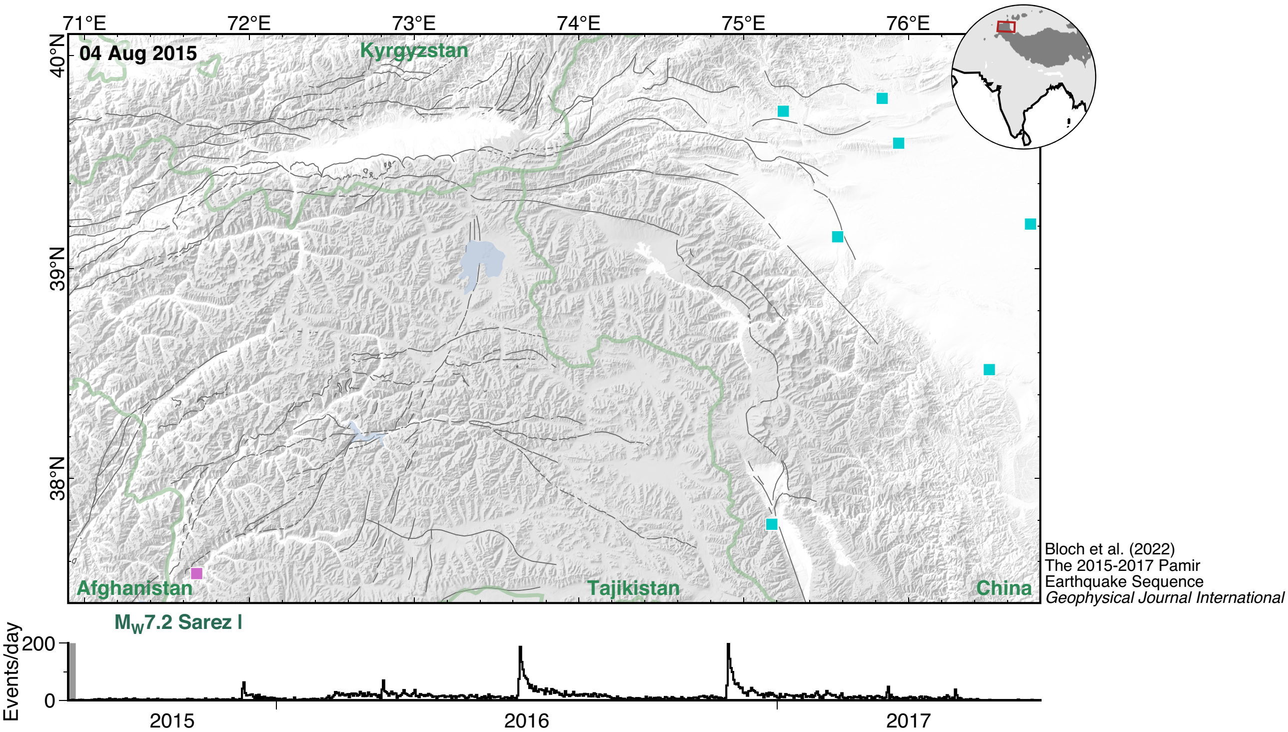

Video 1.

slab retreat is forced by indentation of Indian lithosphere, bulldozing into the lithosphere of the Tajik-Tarim basin at mantle depth. In this context, the SKFS and the two largest earthquakes in the Pamir interior—the December 2015 and the 1911 earthquakes—with similar sinistral strike-slip mechanisms in about the same region, likely express the underthrusting of the northwestern leading edge of the Indian mantle lithosphere indenter. The 2015 Sarez rupture may be the most recent manifestation of the shear zone at the northwestern tip of the indenter, building a continuous fault zone along the indenter's western edge and connecting the distributed sinistral fault zones of the Hindu Kush with the SKFS (Schurr *et al*. 2014; Metzger *et al*. 2017; Kufner *et al*. 2018, 2021).

3 SEISMOLOGICAL DATA AND METHODS

3.1 Data

We operated the East Pamir seismic network (FDSN code 8H; Yuan *et al*. 2018a) with 30 sites in the eastern Pamir, northwestern Kunlun and northwestern Tarim Basin between August 2015 and July 2017, and the Sarez-Pamir aftershock seismic network (FDSN code 9H; Yuan *et al*. 2018b) with 10 sites on the Pamir Plateau between February 2016 and July 2017 (Fig. 1a). We used additional seismic waveform data from the Xinjiang regional seismic network (SEISDMC 2021) and the Tajik National Seismic Network (FDSN code TJ; PMP International (Tajikistan) 2005).

We detected 39 309 seismic events using the *Lassie* earthquake detector as coherent peaks in move-out corrected, smoothed, pulse-like seismogram image functions that were stacked on a rectangular grid of 100× 100 ×10 trial subsurface points with a spacing of 10× 10 ×30 km (Comino *et al*. 2017) using the 1-D velocity model of Sippl *et al*. (2013b). The initial location and predicted *P*- and *S*-wave arrival times were used as a starting point for phase arrival time picking. We picked *P*-wave arrival times automatically with *MannekenPix* (Aldersons 2004), where *obspy*'s STA/LTA triggers and predicted arrivals from the detection routine were used as starting points; *S*-wave arrival times were picked with *spicker* (Diehl *et al*. 2009). Filter window lengths and positions for both algorithms were calibrated with manually picked phase arrivals of 59 events. After each picking run, events were located with *hypo71* (Lee & Lahr 1972), and arrival times with the highest residuals were removed until the location RMS misfit fell below a threshold of 2 s for *P* waves and 3 s for *P* and *S* waves combined. We then used a subset of 1855 seismic events with the best constrained arrival-time picks to invert for a 1-D velocity model and static station corrections using *velest* (Kissling *et al*. 1994). We removed arrival times that yielded a residual five times larger than the standard deviation of all residuals of a certain seismic phase on a certain station, resulting in preliminary locations for 29 795 events. We excluded 20 apparent high-RMS misdetections (e.g. teleseismic events or network-wide null data in the XJ network), 13 149 events with less than 6 arrival time picks, 9366 events with an azimuthal gap larger than 270° and 810 events below 300 km depth. Some events were removed due to more than one criterion. We manually revised the picks of 82 events of special interest, such as main shocks or major foreshocks. After this step, we located 11 782 seismic events in the 3-D *P*-wave velocity model of Bloch *et al*. (2021) with *simulps* (Thurber 1983). We computed waveform cross-correlation differential arrival times of event pairs less than 10 km apart with *obspy* (Krischer *et al*. 2015) and determined refined relative event locations for 3748 events using differential *P*- and *S*-wave catalogue- and cross–correlation-arrival–times in *hypoDD* (Figs S1–S3; Waldhauser & Ellsworth 2000). The depth of 2352 likely shallow events could not be resolved. They are located at the surface (i.e. the top boundary of the velocity model at –3 km); their map view distribution is similar to events with well-constrained depths, giving us confidence that they do not bias the overall seismicity pattern (Bloch *et al*. 2022).

3.2 Regional moment tensors

We determined regional moment tensors using the *RMT* algorithm of Nábělek & Xia (1995). Green's functions were computed with the discrete wavenumber summation method of Bouchon (1981) from the velocity and damping structure, previously obtained by Sippl *et al*. (2013b; Fig. S4). Seismograms were bandpass filtered per event at the lowest possible frequencies still providing a good signal. For most events, filter corners of 20 and 60 s were suitable. Only events 2, 5 and 7 (Table 1) were filtered with a broader pass band between 15 and 80 s, and events 1, 3 and 7 with a narrower one between 10 and 40 s. Noisy waveforms were discarded interactively. We allowed small timing adjustments between observed and synthetic seismograms to match the phase. In total, we were able to retrieve 33 moment tensors of events with moment magnitude M_W between 4.0 and 6.0 (Table 1; Bloch *et al*. 2022). Moment tensors of the three large main shocks could not be computed due to clipped waveforms; we instead report the moment tensor and magnitude published by the National Earthquake Information Center (NEIC).

A comparison between moment tensors and magnitudes of 10 events that were also analysed by NEIC shows that the focal mechanisms agree (Fig. S5a). Significant differences occur only for two events from the Sary-Tash aftershock sequence (8 and 11 in Fig. S5a). Within the context of other similar mechanisms in the sequence, the good waveform fit (Figs S6 and S7), and given our better database, we are confident in our solutions.

3.3 Magnitudes

Calibrated local magnitudes M_L were obtained for all events by investigating the largest horizontal ground displacement amplitude A as a function of distance R. Following Bormann & Dewey (2012), we corrected the seismograms for their respective instrument response function and convolved them with the one of a Wood–Anderson seismograph. We measured the largest amplitude of any of the horizontal components and calibrated the magnitude–amplitude–distance relationship (Bormann & Dewey 2012):

$$M_L^i = \log_{10} A^i + B \log_{10} R^i + C R^i + D \quad (1)$$

by minimizing:

$$\epsilon = \frac{1}{N} \sum_{i=1}^{N} \sqrt{\left(M_L^i - M_W^i\right)^2} \quad (2)$$

for all 921 station observations i of the 33 events for which M_W is available (Fig. S5c). We report the so calibrated M_L as the mean value of M_L^i after removal of outliers.

We computed the magnitude of completeness M_c of the entire catalogue as the lower end of the longest linear segment of the cumulative frequency–magnitude distribution (Fig. S5d). A daily minimum completeness magnitude M_c^{min} was computed as the most frequent magnitude (binned in intervals of 0.1) observed in the previous 60 d (Woessner & Wiemer 2005).

4 SEISMICITY

Fig. 2 shows different representations of the spatio-temporal seismicity pattern. In the following, regions of distinct seismic activity are denoted with capital letters *A*–*I*. They are defined as rectangular areas around the three largest main shock fault zones (*A*, *C*, *E*) and 15 km radii around the more moderate main shocks (*B*, *D*, *F*–*I*) down to 50 km depth (Fig. 2a). The largest earthquake within each volume, specifically its hypocentral location and time, is denoted with an asterisk (A^*–I^*). Foreshocks are events that occurred in the so-defined volumes before the respective main shock. Important foreshocks are denoted with a prime symbol (*c'* and *e'*).

Seismicity in the studied time period was high and modulated by the occurrence of the three major earthquakes, which mark peaks in the detected earthquake rate (Figs 2b and c; Video 1) at an overall magnitude of completeness $M_c = 2.3$ (Fig. S5d). The Sarez main shock A^* and early aftershocks occurred when only the 8H seismic network was in operation. Hence, the magnitude of completeness was relatively high in the main shock area ($M_c^{min} \approx 2.5$, Fig. 2d), compared to the eastern Pamir and Tarim basin area ($M_c^{min} \approx 1.6 - 2$). The installation of the 9H network in February 2016 on the Pamir Plateau increased the sensitivity of the entire network significantly ($M_c^{min} \approx 1.8$), even though high aftershock productivity deteriorated the detection threshold at times ($M_c^{min} \approx 2.2$). Other peaks in the event rate are due to the largest aftershock of the Sarez earthquake (B^*), an earthquake swarm in the western Pamir (*D*) and M_W 4–5 earthquakes near Yarkant (F^*), Khorog (G^*), Karamyk (H^*) and Taxkorgan (I^*; Figs 2a and c; Table 1).

The main shocks B^*–H^* following the Sarez earthquake sequentially activated fault zones at increasing epicentral distance r from the centroid location of the Sarez earthquake (Fig. 2e and S8). The time of the fault activation is approximately enclosed in an envelope function of the form of a diffusion equation (Shapiro *et al*. 1997, 2003):

$$r = r_0 + \sqrt{2\pi D(t - t_0)}, \quad (3)$$

where r_0 is the distance from the Sarez centroid to the northern or southern end of the rupture, t_0 is the main shock origin time (Table 1) and D is a scaling constant that may be interpreted as hydraulic diffusivity. The sequential activation is not observed in the foreshock activity (Figs 2c and e). The fault volumes *A*, *B*, *C*, *D*, *E* and *G* were seismically active before the respective main shocks—even years before, as recorded by the local TIPAGE seismic network (Schurr *et al*. 2014). This makes the distinction between foreshocks and background seismic activity only possible in retrospect. It is also not evident that the foreshock activity was triggered, enhanced, or diminished by any main shock. Some rupture volumes showed phases of increased foreshock activity (*C* in February and April 2016, *E* in May and August 2016; Fig. 2c) and aftershock rates (*C* in August 2016, *E* in February 2017; Fig. S9). However, these phases do not correlate spatially, but rather represent subordinate aftershock sequences. Only volume *B* of the largest Sarez aftershock, which occurred ∼25 km from the Sarez epicentre, started to become seismically active immediately after the Sarez main shock. The aftershock rate n of the main sequences generally follows the modified Omori–Utsu law (Utsu *et al*. 1995):

$$n(t) = \frac{K}{(t + c)^p} \quad (4)$$

with the time after the main shock t, aftershock productivity K, time lag c and decay parameter p. We note that the variability in p is high. It lies between ∼1.15 for sequences *B* and *E* and up to 1.5 for sequence *G* (Fig. S9).

Table 1. Source parameters and failure stresses of the large and moderate earthquakes for which a moment tensor is available. Strike, dip and rake of our preferred fault plane. # denotes our moment tensors shown in Fig. 3; Sequence (Seq.) denotes the studied earthquake sequence, defined in Fig. 2; *denotes the largest earthquake of the sequence. Depth is centroid depth, except for the three largest main shocks, for which we report hypocentral depths. The change in Coulomb failure stress (ΔCFS) is due to all previous earthquakes. For *c'* and *C**, ΔCFS without possible creep on the SKFS (Fig. 8) is given in brackets. Large negative ΔCFS in parenthesis are artefacts of the too coarse fault-slip models that lack small scale slip heterogeneities.

#	Seq.	Name	Time	M_W (°E)	Lon. (°N)	Lat. (km)	Depth (°)	Stike/Dip/Rake (kPa)	ΔCFS
	A*	Sarez	2015-12-07 07:50:04	7.2[a]	72.853	38.223	0.9	214/83/8[a]	0^{+0}_{-0}
1	A		2015-12-07 10:34:22	4.4	72.904	38.289	9.0	26/81/24	(-425^{+345}_{-295})
2	A		2015-12-07 15:23:56	4.6	73.225	38.719	4.0	198/40/344	(-189^{+122}_{-169})
3	B		2015-12-27 23:05:28	4.2	72.697	38.069	6.0	181/40/234	$+27^{+52}_{-34}$
4	A		2016-01-13 21:37:37	4.8	73.322	38.742	9.0	225/40/338	$+102^{+65}_{-38}$
5	B*		2016-03-18 16:11:00	5.3	72.618	38.003	4.0	219/68/5	$+132^{+70}_{-56}$
6	B		2016-03-21 05:32:27	4.1	72.581	38.002	4.0	230/38/325	(-306^{+124}_{-108})
7	c'		2016-04-09 16:19:33	4.4	73.502	39.428	9.0	79/50/157	$+4^{+2}_{-2}$ $[+8^{+3}_{-3}]^{d}$
	C*	Sary-Tash	2016-06-26 11:17:08	6.4[a]	73.411	39.462	11.9	266/67/126[b]	$+4^{+4}_{-3}$ $[+3^{+4}_{-5}]^{d}$
8	C		2016-06-27 06:25:37	4.6	73.463	39.438	12.0	278/55/120	(-434^{+198}_{-270})
9	C		2016-06-27 07:34:13	4.3	73.657	39.447	6.0	123/37/194	$+499^{+160}_{-138}$
10	C		2016-06-27 19:28:49	4.8	73.544	39.441	15.0	265/33/93	(-2007^{+516}_{-671})
11	C		2016-06-28 12:43:16	4.7	73.499	39.456	15.0	292/28/182	(-596^{+354}_{-340})
12	C		2016-06-28 21:38:04	5.4	73.412	39.440	15.0	91/80/163	$+111^{+251}_{-288}$
13	C		2016-06-29 08:08:14	4.5	73.471	39.443	12.0	287/52/139	(-791^{+225}_{-249})
14	A		2016-06-30 07:09:43	4.2	72.930	38.426	18.0	217/82/320	(-1038^{+348}_{-385})
15	C		2016-07-01 11:01:14	4.0	73.733	39.449	6.0	134/33/222	$+335^{+91}_{-110}$
16	C		2016-07-04 02:24:20	4.4	73.525	39.446	9.0	308/81/186	-9^{+96}_{-120}
17	A		2016-07-08 12:10:25	4.1	72.840	38.085	4.0	49/88/306	(-82^{+221}_{-223})
18	C		2016-07-21 05:29:20	4.5	73.527	39.450	6.0	238/81/73	(-393^{+111}_{-125})
19	D		2016-08-04 21:34:41	4.1	72.568	38.877	4.0	352/69/263	$+33^{+20}_{-14}$
20	D		2016-08-04 23:42:17	4.4	72.548	38.868	4.0	350/71/264	$+10^{+18}_{-18}$
21	D*		2016-08-14 15:05:20	4.6	72.590	38.858	6.0	329/72/234	$+18^{+13}_{-10}$
22	D		2016-08-14 15:11:39	4.2	72.584	38.838	4.0	22/66/287	$+103^{+24}_{-26}$
23	e'		2016-11-25 14:18:59	5.0	74.034	39.267	15.0	291/68/173	-13^{+5}_{-9}
	E*	Muji	2016-11-25 14:24:27	6.6[a]	74.039	39.269	13.7	106/88/184[c]	$+59^{+157}_{-172}$
24	E		2016-11-25 19:46:19	4.2	74.295	39.198	6.0	292/77/192	(-2072^{+762}_{-784})
25	E		2016-11-26 09:23:26	5.0	74.274	39.202	6.0	293/80/224	(-1175^{+501}_{-371})
26	E		2016-12-19 10:57:33	4.4	74.047	39.256	15.0	290/59/160	(-540^{+522}_{-363})
27	F*	Yarkant	2017-01-20 09:54:08	5.0	76.653	38.292	12.0	176/25/121	0^{+0}_{-0}
28	A		2017-03-14 11:07:11	4.8	73.455	39.249	12.0	191/84/351	$+23^{+19}_{-28}$
29	G*	Khorog	2017-03-22 11:27:02	4.9	72.084	37.668	12.0	238/88/8	$+12^{+4}_{-5}$
30	H*	Karamyk	2017-05-03 04:47:13	6.0	71.510	39.542	15.0	251/74/178	-3^{+1}_{-1}
31	H		2017-05-05 05:09:35	5.7	71.514	39.532	12.0	237/48/115	(-1210^{+318}_{-430})
32	I*	Taxkorgan	2017-05-10 21:58:21	5.4	75.305	37.627	6.0	317/60/247	$+0^{+0}_{-0}$
33	C		2017-05-22 09:23:09	4.5	73.645	39.409	4.0	60/72/89	(-1356^{+348}_{-361})

[a]NEIC; [b]He *et al*. (2018); [c]Bie *et al*. (2018); [d] without creep (Fig. 8).

Crustal seismicity that is not associated with any of the main shocks delineates known neotectonic structures (Figs 1, 2a and 3): the MPTS exhibited diffuse seismic activity; the Kongur Shan Normal Fault System was seismically active between the Muji Fault and the northern end of the Taxkorgan Fault; the Aksu–Murghab Fault Zone was active along a swath in the southcentral Pamir. In the following, we investigate the main shock volumes, providing a detailed seismotectonic framework for the active deformation field of the Pamir.

5 SEISMOTECTONICS

5.1 Sarez earthquake

The 2015 M_W 7.2 Sarez earthquake (*A** in Figs 2 and 4; Table 1) ruptured an ∼80-km-long part of the SKFS between Lake Sarez and the Kokujbel Valley south of Lake Karakul (Figs 3 and 4; Metzger *et al*. 2017; Sangha *et al*. 2017; Elliott *et al*. 2020). Metzger *et al*. (2017) divided the rupture plane into three segments

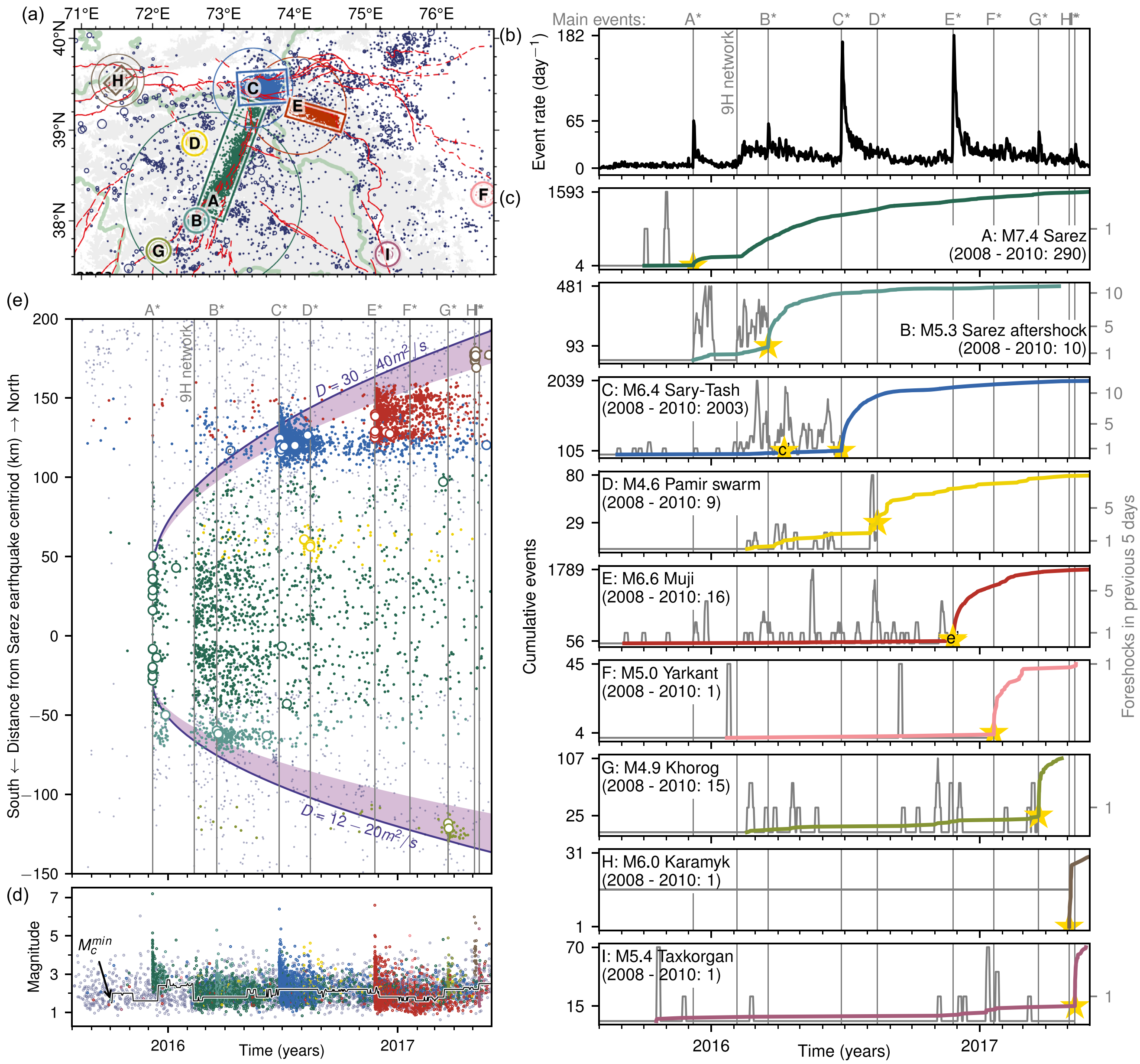

Figure 2. Spatio-temporal evolution of seismic activity. (a) Spatial definitions of sequences (*A* to *I*) with earthquakes colour-coded as in the other subfigures and Fig. 3. See Video 1 for an animated and sonified version. (b) Seismic event rate over time. (c) Cumulative event number inside each sequence (coloured) and 5-d moving window event number before the main shock for each sequence (grey); event with largest magnitude in sequence is marked with a star and labelled on top. The number in the sequence of the strongest and the last event is labelled on the left. Cumulative event number from 2008 to 2010 for the specific region in parenthesis from Schurr *et al*. (2014). For aftershock event rate, see Fig. S9. (d) Magnitude over time with time variable minimum magnitude of completeness ($M_c^{\min}$). (e) Spatio-temporal distribution of the seismic events with respect to the M_W7.2 Sarez earthquake centroid. $M_W > 4$ events are highlighted as larger circles. The activation of the main shock rupture planes mimics the diffusion eq. (3) with scaling constant *D* (Fig. S8). Most of the future main shock volumes show foreshock activity, but foreshock activity is independent of main shocks on other faults.

distinguished by strike changes (Fig. 4a). The northern part of the southern segment showed swarm-like seismic activity with 290 events detected during the August 2008 to July 2010 TIPAGE deployment (Fig. 4b; Sippl *et al*. 2013b). The swarm had ceased in August 2015, with only one M_L 2.4 event detected on the fault in the 4 months before the Sarez main shock (Fig. 4b, ∼20 km from the hypocentre). The relative seismic quiescence before the main shock and a magnitude of completeness $M_c^{\min} \approx 2.0 - 2.5$ (Figs 2c and d) suggest that no significant foreshock occurred before the Sarez earthquake.

The aftershocks of the Sarez earthquake skirted around the coseismic slip patch. In both continuations of the slip patch, northward and southward, the earliest (∼1.5 d) aftershocks appear to migrate away from the tip of the rupture at a constant velocity of between 0.5 and 2 km hr^{-1} (Fig. S8). Comparable earthquake migration velocities have been interpreted as a signature of propagating slow slip after a large earthquake (Kato *et al*. 2016) or inside earthquake swarms (Roland & McGuire 2009; Shimojo *et al*. 2021). Later aftershocks were concentrated at the northern end of the rupture (Fig. 4c; ∼60 km from the hypocentre) with sinistral transtensional

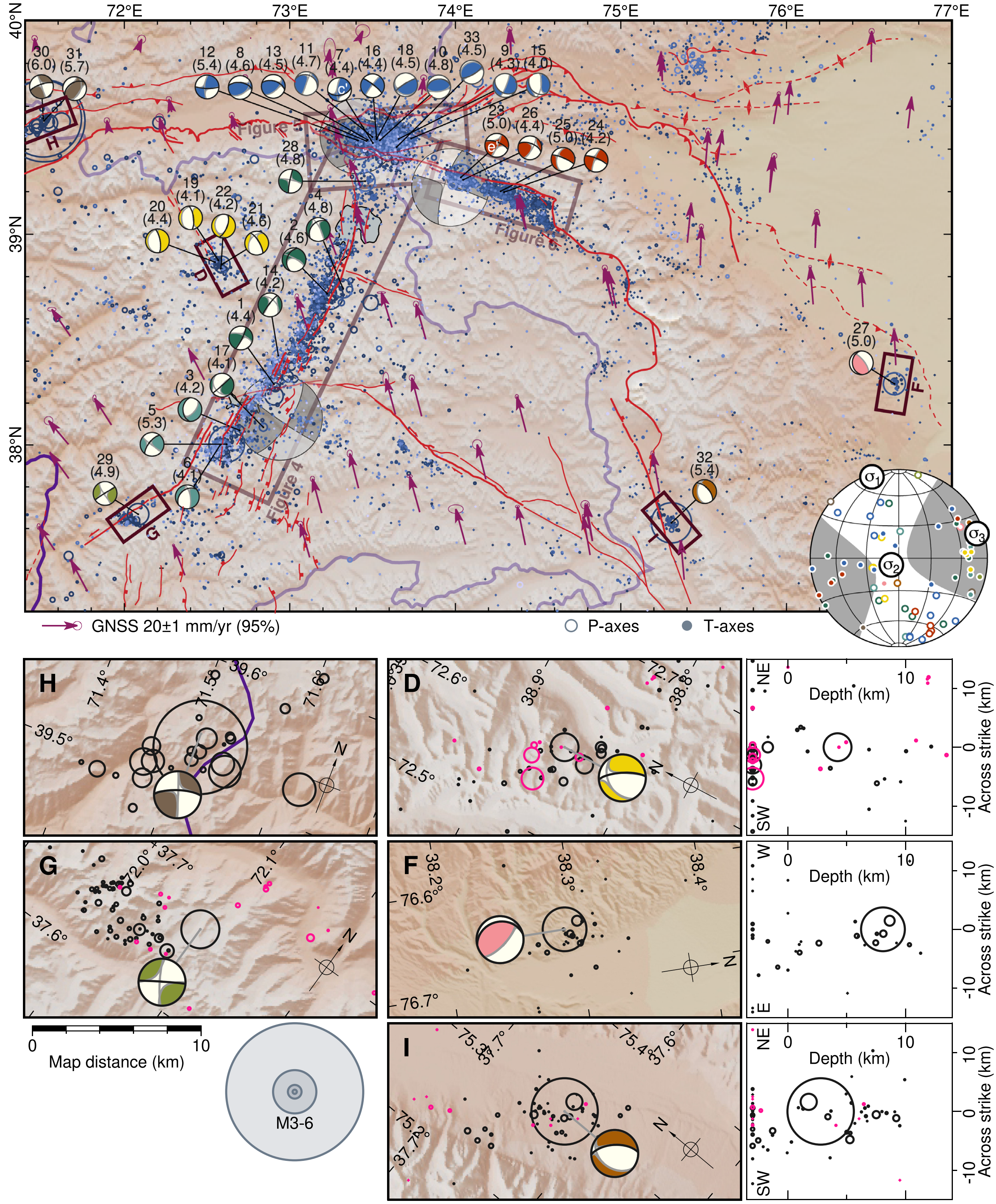

Figure 3. Summary of moment tensor results. Moment tensors coloured by earthquake sequence as in Fig. 2 and numbered as in Table 1. M_W given in parenthesis. Interpreted fault planes are marked in the beach balls in black; fault planes preferred by stress inversion are marked in the beach balls in dark grey; auxiliary plane in light grey. Top panel: regional overview map. GNSS vectors from Zubovich *et al.* (2010) and Ischuk *et al.* (2013). Major neotectonic faults in red. Bottom panel: close-ups for sequences framed in the top subfigure; foreshocks (magenta); main shock and aftershocks (black). (*H*, *G*) map views. (*D*, *F*, *I*) with additional across-strike profiles. Inset: stereographic projection of moment and stress tensor principal axes. Positive areas of the stress tensor are shaded. Lower hemisphere stereographic projection.

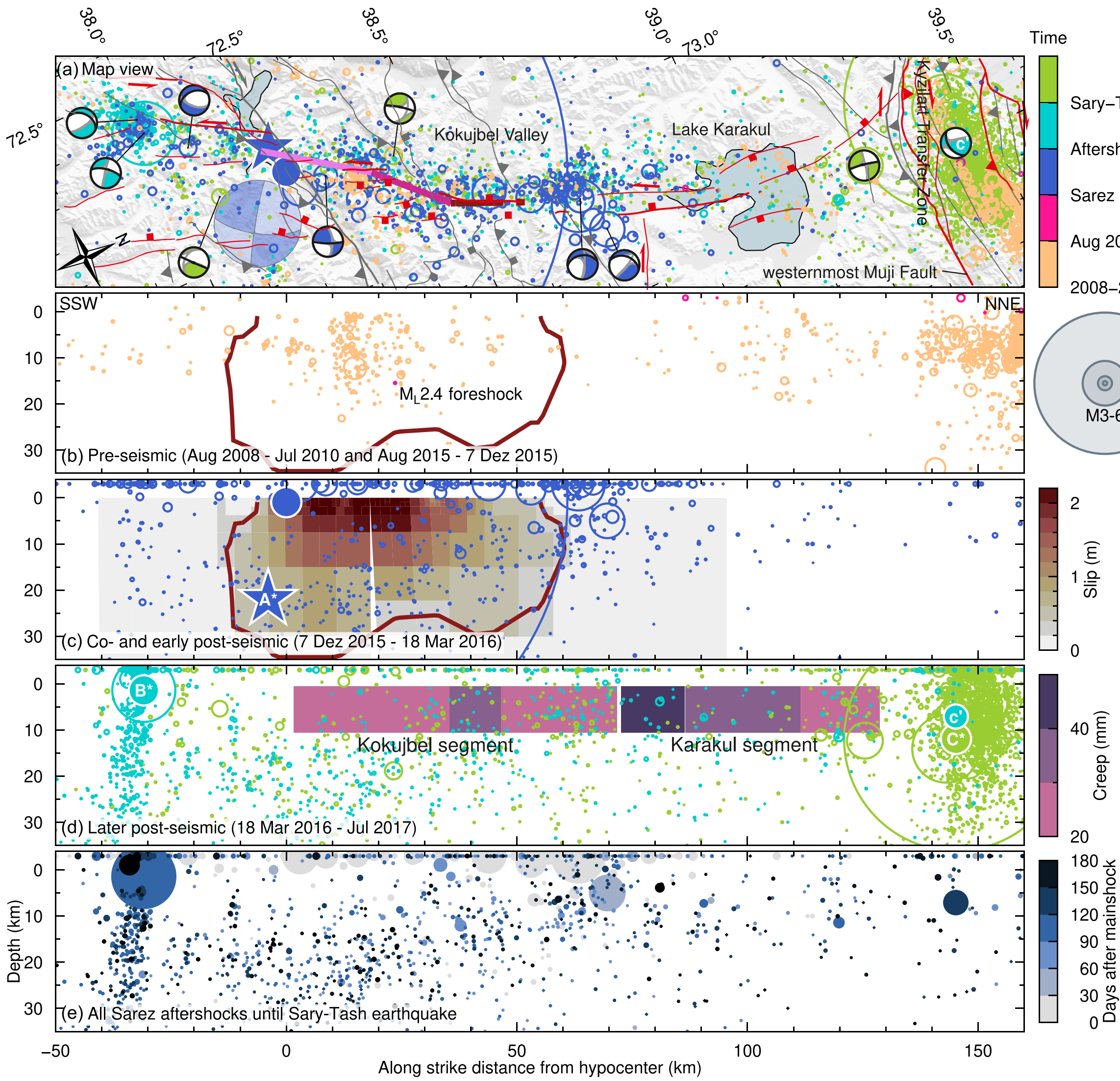

Figure 4. Time succession of seismicity and moment tensors of moderate earthquakes in the active part of the Sarez-Karakul Fault Zone; GEOFON focal mechanism of the main shock (large beach ball); preferred hypocentre location by NEIC (star); 2008–2010 seismicity from Schurr *et al.* (2014). (a) Along-strike map view with the three segments of the coseismic rupture highlighted (Metzger *et al.* 2017). Mapped Cenozoic structures in grey and neotectonic structures in red. Beach ball representation of moment tensors (Table 1) with preferred fault plane in black. (b–d) Along strike profiles. (b) Seismicity before the Sarez main shock. 10 per cent of maximum future slip contoured. (c) Early aftershock seismicity until aftershock B^*. Coseismic slip from Metzger *et al.* (2017). (d) Later aftershock seismicity. Cumulative creep model as in Fig. 8 between A^* and C^* (Table 1). (e) Time succession of the Sarez aftershocks until the Sary-Tash earthquake. The larger ($M > 4$) earthquakes migrated away from the main shock rupture. No significant immediate foreshock activity was detected for the Sarez earthquake. The rupture plane has been constantly active throughout 2008–2010. Aftershock seismicity skirts around the coseismic slip patch.

focal mechanisms (Fig. 4a) and ∼20 km south of the end of the coseismically active fault patch (Fig. 4c; –30 km). This was where the largest M_W 5.3 aftershock B^* occurred, with a sinistral strike-slip mechanism similar to the Sarez main shock, 102 d after the main shock. It spawned its own aftershock series (Figs 2c, 3 and 4d). An area of relative seismic quiescence between the southern end of the Sarez rupture and aftershock B^* (between 10 and 30 km south of the Sarez hypocentre A^*, Fig. 4d) may be attributed to the 1918 M_W 6.6 earthquake that could have relaxed this segment (Fig. 1b; Bondár *et al.* 2015).

The associated moment tensors exhibit both sinistral strike-slip and normal faulting mechanisms. Neither the coseismic nor the post-seismic activity reactivated the ∼E-striking, Cenozoic thrusts and normal faults of this part of the Pamir (Fig. 4a). The ∼NNE-strike of the normal-fault nodal planes are parallel to the many tensional surface-breaks mapped on ground along the northern segment (fig. 6 of Metzger *et al.* 2017) and the Quaternary-filled grabens, outlined on the 1:200 000 geological maps and traceable from topography (Fig. 4a; Yushin *et al.* 1964). An important event of the earthquake sequence was the 9 April 2016 M_W 4.1 dextral strike-slip foreshock *c'* that occurred 124 d after the Sarez main shock, ∼85 km north of the tip of its rupture plane and 78 d before and ∼10 km east of the hypocentre of the Sary-Tash earthquake (Figs 2c, 4d and 5).

5.2 Sary-Tash Earthquake

The Sary-Tash earthquake (C^* in Figs 2–5; Table 1) occurred within the MPTS, westerly adjacent to the 2008 M_W 6.6 Nura earthquake (Schurr *et al.* 2014; Sippl *et al.* 2014; Teshebaeva *et al.* 2014;

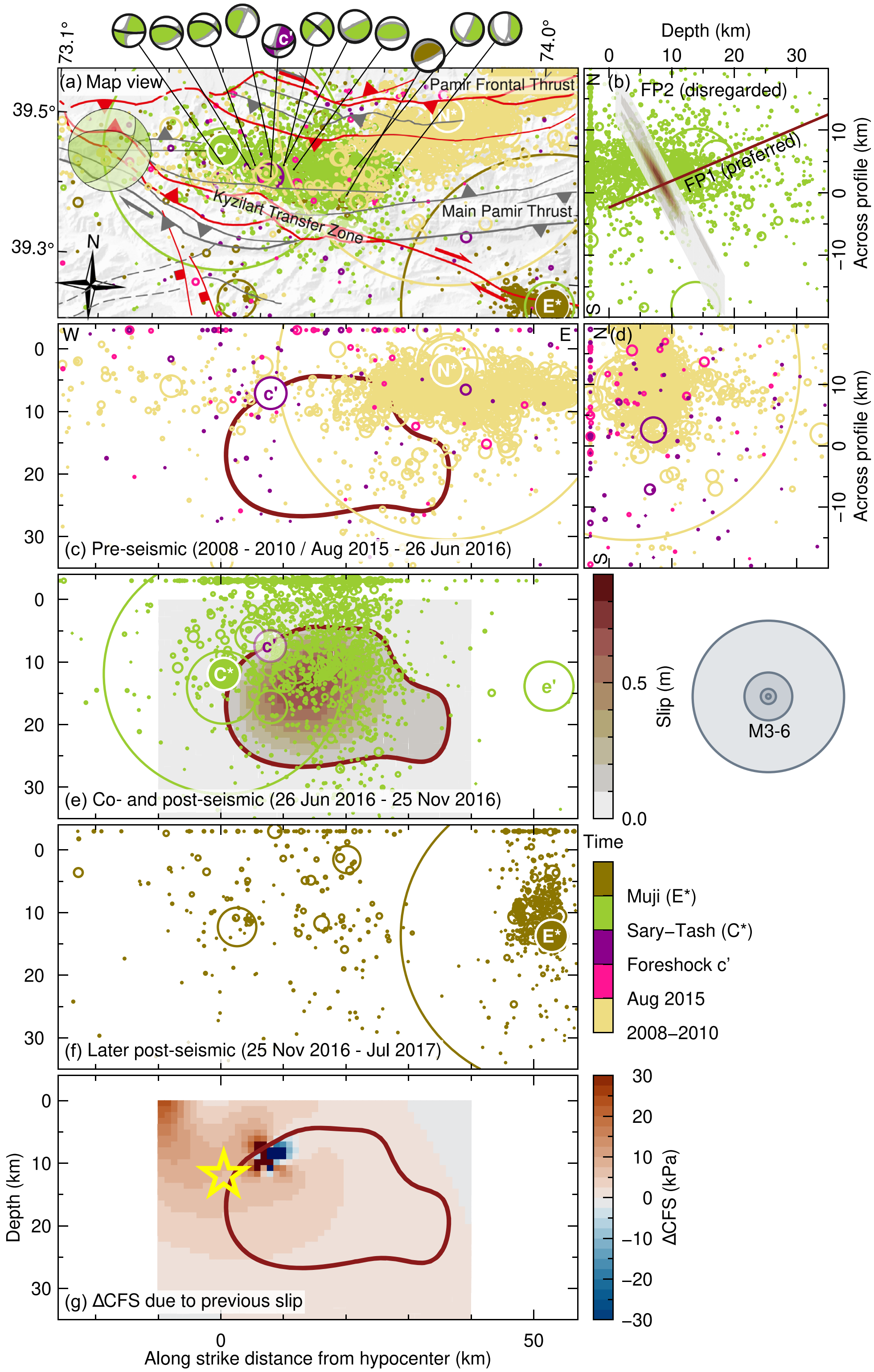

Figure 5. Time succession of seismicity and moment tensors of moderate earthquakes in the active part of the Main Pamir Thrust System; GEOFON focal mechanism of the main shock (large beach ball); 2008–2010 seismicity from Schurr *et al.* (2014); hypocentre of the 2008 Nura earthquake (N^*; Sippl *et al.* 2014) and fore- and main shocks discussed in the text (c', C^*, e', E^*). (a) Along-strike map view. Mapped Cenozoic structures in grey and neotectonic structures in red. Beach ball representation of moment tensors (Table 1) with preferred fault plane in black. (b, d) Across-strike profiles. (c, e, f) Along-strike profiles. (b) Aftershock seismicity and the two possible fault planes of the main shock (He *et al.* 2018). FP1 is preferred, because aftershock seismicity concentrates in the hanging wall. (c, d) Seismicity before the Sary-Tash main shock; 10 per cent of maximum future slip contoured. (e) Early aftershock seismicity until subsequent Muji main shock E^*. Coseismic slip from He *et al.* (2018). (f) Later aftershock seismicity and spatial configuration with the Muji earthquake (E^*). (g) ΔCFS on the fault plane. Star marks the hypocentre. Foreshock activity left out the future rupture area and grossly concentrated around the future hypocentre since c'. Note the lesser depth extent of the Nura aftershock seismicity.

Qiao *et al*. 2015). The region—geologically poorly mapped in the high-altitude terrain of the Tajikistan–Kyrgyzstan–China border triangle—is characterized by a complex network of faults with both ∼N- and ∼S-dips, making the choice of the fault plane from the two nodal planes non-trivial. NEIC reports a comparatively low double-couple component for the main shock moment tensor of 86 per cent, hinting at the complexity of the rupture process.

The earthquake volume partially overlaps with the aftershock volume of the 2008 Nura earthquake (Sippl *et al*. 2014) and was seismically active throughout the different deployment periods of the various seismic networks covering the region; 13 small earthquakes (M_L 1.6–3.7) were detected in the vicinity of the future Sary-Tash earthquake in the 2 months preceding the 2008 Nura earthquake during the TIPAGE deployment and 188 (M_L 1.0–M_W 4.4) in the 11 months before the Sary-Tash earthquake since the 8H network was active (Figs 2c, 5c and d). Foreshock activity was high compared to the Sarez and Muji sequences and peaked in three ∼1-month-long swarms in March, April, and June 2016 (Fig. 2c). Notably, the events that followed the 9 April 2016 foreshock *c'* concentrated around the future hypocentre C^* in along-strike view (Fig. 5c). The aftershocks of the Sary-Tash earthquake outlined an about vertical, ∼E-striking structure to ∼20 km depth east of the hypocentre (Figs 5b and e). Moment tensors display a variety of focal mechanisms, again testifying to a complex fault-zone (Figs 3 and 5a).

Fault-slip models of InSAR displacement maps slightly favour the steeply N-dipping nodal plane (FP1) over the gently ∼*S*-dipping one (FP2) for the Sary-Tash main shock (He *et al*. 2018). If FP2 was the main fault plane, the aftershocks would crosscut it and be concentrated inside the volume of the largest slip (Fig. 5b). This is contrary to what is observed for the Sarez (Section 5.1) and Muji (Section 5.3) earthquakes, and many other earthquakes worldwide, where aftershocks concentrate *around* the segments of highest slip (Das & Henry 2003). We prefer the ∼N-dipping FP1 as the main fault plane, because with this choice the aftershocks are located in the hanging wall and updip of the largest coseismic slip (Fig. 5b), a pattern that has also been observed for the 2008 Nura earthquake (Sippl *et al*. 2014). The hypocentre is located at the western end of the geodetically determined coseismic slip patch (He *et al*. 2018), at 11.9 km depth, to the west and at 8.6 km hypocentral distance to the M_W 4.4 foreshock *c'* (Fig. 5e). The variable aftershock focal mechanisms tend to have dextral-transpressive mechanisms on ∼E-striking planes, except for two normal faulting events at the eastern end of the rupture (Fig. 5a). The ∼E-striking nodal planes of the strike-slip solutions are interpreted to carry the dextral strike-slip deformation identified in the background seismicity of the TIPAGE deployment data and by geological fault-slip analysis within the MPTS and in the Kyzilart Transfer Zone; even the normal-fault earthquakes, indicating E–W extension, have neotectonic fault equivalents, and were interpreted as interaction of the SKFS with the MPTS (Sippl *et al*. 2014). The hypocentre depth and presumed N-dip of the Sary-Tash earthquake fault suggest that a basement fault in the footwall of the Pamir Frontal Thrust got re-activated that intersects ∼4 km thick Devonian passive margin carbonates. Such basement faults are common in the Tian Shan immediately to the north (Fig. 1b). In contrast, the 2008 Nura earthquake ruptured a ∼S-dipping plane; its hypocentre lay at 3.4 km depth and thus likely in the MPTS imbricate stack. That the Sary-Tash and Nura aftershock activities hardly overlap along strike, occupy different depth intervals, and differently dipping patches indicate that they activated different faults (Figs 5c and d). Another difference is that the shallow Nura earthquake re-activated several pre-existing NE- and NW-striking faults in the Tian Shan during its regionally extensive aftershock sequence; the deeper Sary-Tash earthquake did not.

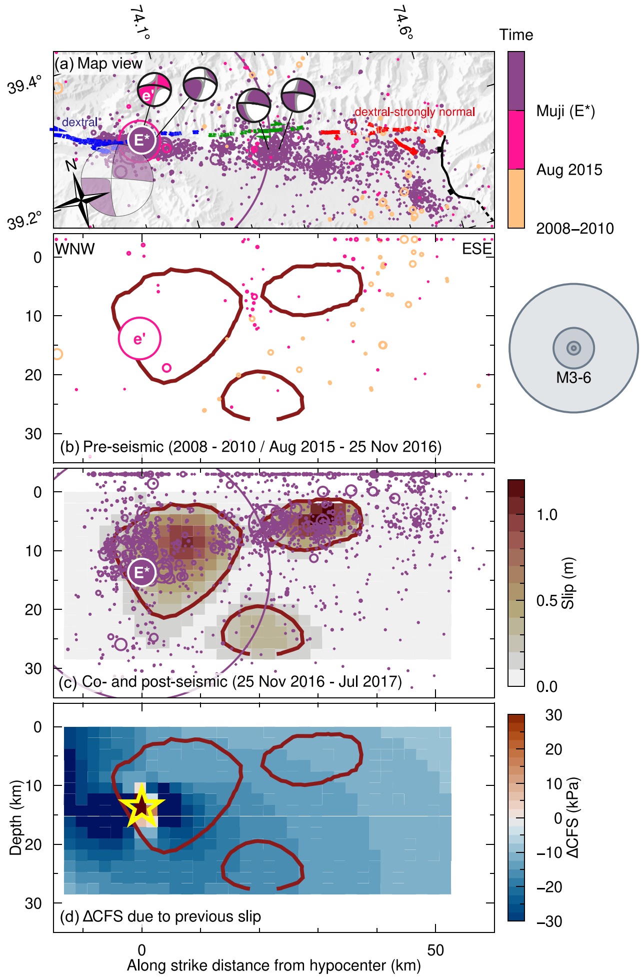

Figure 6. Time succession of seismicity and moment tensors of moderate earthquakes in the active part of the Muji Fault; GEOFON focal mechanism (large beach ball); 2008–2010 seismicity from Schurr *et al*. (2014); fore- and main shock hypocentres (*e'*, *E**). (a) Along-strike map view. Beach ball representation of moment tensors (Table 1) with preferred fault plane in black. Surface traces (blue, green, red) of the Muji-Fault earthquake and other faults modified from Li *et al*. (2019) (b, c) Along-strike profiles. (b) Seismicity before the main shock; 10 per cent of maximum future slip contoured, the lowermost slip patch is not resolved. (c) Aftershock seismicity and coseismic slip model (Bie *et al*. 2018). (d) ΔCFS model due to all previous earthquakes. Star: earthquake hypocentre. Foreshock activity left out the future rupture area. *e'* occurred 12 min before the main shock, very close to the hypocentre location. Stress transfer from the previous earthquakes acted stabilizing on the fault plane.

5.3 Muji earthquake

153 d after the Sary-Tash earthquake, the M_W 5.0 foreshock to the Muji earthquake *e'*, and its main shock E^* occurred on the Muji Fault, ∼35 km southeast of the end of the rupture plane of the Sary-Tash earthquake. This configuration likely connects the MPTS in the area of the Sary-Tash earthquake with the Muji Fault along the Kyzilart Transfer Zone.

The rupture plane of the 2016 M_W 6.6 Muji earthquake (E^* in Figs 2, 5 and 6; Table 1) broke nearly simultaneously in two main slip patches; a third slip patch, modelled below ∼20 km depth, is unresolved (Bie *et al*. 2018). The area of the eastern slip patch was seismically active during the TIPAGE (2008–2010) and the current deployment (2015–2017; Fig. 6b). The M_W 5.0 Muji foreshock *e'* occurred only 12 min before the main shock, at the western end of the rupture plane and at ∼460 m hypocentral distance (Figs 6a and b). We identified a series of four more foreshocks between *e'* and E^* in the seismogram of the closest station EP10 but could not locate them. The main shock hypocentre was at 13.7 km depth. Aftershocks concentrated around and below the highest slip zone at the WNW end of the rupture plane, tightly constrained to the rim of the main slip patch; they continued ∼10 km beyond its ESE' end of the eastern slip patch (Fig. 6c). The western continuation of the Muji fault remained seismically quiet.

Fore- and aftershock moment tensors exhibit dextral focal mechanisms similar to the main shock. Notably, the two western focal mechanisms have a small reverse faulting component, while the two eastern ones have a small normal faulting component, a fault kinematic that was also observed in the morphology of the surface breaks (Li *et al*. 2019). This is compatible with the transition from the nearly purely extensional faulting along the Kongur Shan Normal Fault System to the dextral-transpressional Kyzilart Transfer Zone and MPTS.

The occurrence of aftershocks east but not west of the Muji main shock rupture plane may suggest that the western continuation of the Muji Fault was not critically stressed. Either it was relaxed by the sinistral far-field strain of the 2008 Nura and 2016 Sary-Tash earthquakes or because it already slipped in an unrecorded earthquake or an undetected slip transient on the Kyzilart Transfer Zone. A candidate for an earthquake that filled this seismic gap is the 1974 Markansu earthquake (Fig. 1b). It has been located south of (Fan *et al*. 1994) and relocated (Sippl *et al*. 2014) on the Pamir Frontal Thrust, and full-waveform inversion suggests a complex thrust mechanism similar to the 2008 Nura earthquake (Langston & Dermengian 1981). But Burtman & Molnar (1993) advocated for a dextral strike-slip mechanism similar to the Muji earthquake which would be consistent with the expected slip sense on the quiet segment of the Muji fault. Alternatively, the fault segment with the seismic gap may creep aseismically.

5.4 Northwest Pamir Earthquake Swarm

An earthquake swarm of 80 events occurred on the western side of Pamir's Academy of Sciences Range, hosting Pamir's highest peaks (*D* in Figs 2 and 3; Table 1). It was active throughout the deployment of the Sarez aftershock network (Fig. 2c), with an activity peak, including the largest M_W 4.6 event D^*, in August 2016. We do not see an internal fault architecture or a possible expansion or migration pattern of seismicity. Even if such a pattern existed, we could probably not resolve it, due to the lack of close-by stations near the swarm, rendering location uncertainties significant (Fig. S10). Focal mechanisms indicate normal faulting on ∼N(NW)-striking planes. Well-located hypocentres and moment tensor centroids show that most seismicity clustered at shallow depth (≤6 km; Fig. 3). Such normal-faulting solutions are—together with strike-slip solutions—typical for the western Pamir, the part of the Pamir Plateau that shows westward-increasing gravitational collapse of crust into the Tajik Depression (Schurr *et al*. 2014; Kufner *et al*. 2018).

5.5 Yarkant earthquake

On 20 January 2017, an M_W 5.0 earthquake occurred 53 km southwest of Yarkant, Xinjiang (F^* in Figs 2 and 3; Table 1). Three events were detected in its volume *F* before the earthquake—one of them only 55 min before the main shock—and a total of 41 aftershocks. The moment tensor indicates thrusting on either a shallowly or a steeply dipping fault plane. Seismicity aligns along a ∼N-striking structure (Fig. 3), paralleling the topographic slope and the strike of the shallowly dipping nodal plane. We interpret these earthquakes to record top-to-NE thrusting along ∼SW-dipping faults, compatible with the growth of the eastern Pamir into the Tarim Basin (Figs 1 and 3).

5.6 Khorog earthquake

On 22 March 2017, an M_W 4.9 earthquake occurred ∼51 km ENE of Khorog, Tajikistan (G^* in Figs 2 and 3; Table 1). The volume *G* of the earthquake was active throughout the deployment of the 9H network with 24 seismic events detected before the main shock. Whether the structure was activated by the Sarez earthquake—whose hypocentre is located ∼90 km NE of the earthquake—is unclear, because of the limited sensitivity of the network before the 9H network deployment. Two ∼NE-trending streaks of seismicity can be identified in map view; the focal mechanism indicates sinistral strike-slip on a ∼NE-striking fault. The depth of the earthquake is not well constrained due to the limited network coverage (Fig. 3). The earthquake cluster lies along a fault zone classified as likely active by Stübner *et al*. (2013) and Schurr *et al*. (2014) due to linear topographic expressions; the fault zone coincides with the southeastern part of the Pathus-Nemos Fault of Strom (2014); it overprints the Miocene dextral-normal Gund shear/fault zone at an acute angle (Fig. 1b; Worthington *et al*. 2020). As a mappable continuation of the neotectonic fault network at the southern continuation of the SKFS (Fig. 1b), we interpret the Khorog earthquake cluster as part of the distributed faults that connect the SKFS with the sinistral fault zones of the Hindu Kush (e.g. the Chaman, Panjshir, Central Badakhshan Fault Zones; Fig. 1b), outlining a continuous fault zone along the western edge of the Indian indenter at mantle depth (Section 2; Metzger *et al*. 2017).

5.7 Karamyk earthquake

An M_W 6.0 earthquake happened on 3 May 2017 near the Kyrgyz-Tajik border, ∼25 km west of the settlement of Karamyk, Kyrgyzstan (H^* in Figs 2 and 3; Table 1). The event was outside of the network, but due to the relatively large magnitude some aftershock seismicity could be located and the moment tensors of the main shock and one aftershock could be determined. The seismicity outlined a ∼NE-trending cluster, with a dextral strike-slip- and a reverse-faulting focal mechanism for the main shock and the aftershock, respectively (Fig. 3). The cluster lies along a Cenozoic fault zone in the Tian Shan, outlined by partly overthrusted Jurassic–Palaeogene basin strata; geological fault-slip analysis along the eastern strands of these fault zone reveals top-to-NW thrusting with a dextral strike-slip component (stations TS19–TS22 in fig. S7 in Kufner *et al*. 2018).

5.8 Taxkorgan earthquake

The last moderate earthquake detected during our recording period was the M_W 5.4 Taxkorgan earthquake on 10 May 2017, ∼23 km south of Taxkorgan, Xinjiang (I^* in Figs 2 and 3; Table 1). Aftershock seismicity and the focal mechanism indicate that it reactivated a steeply ∼ENE-dipping segment of the Taxkorgan Normal Fault

(Robinson *et al*. 2007). 14 foreshocks preceded the earthquake, half of them in the 2 months after the Muji earthquake (Figs 2 and 3). The Taxkorgan Normal Fault can be interpreted as part of the Kongur Shan–Taxkorgan Normal Fault System, with a southward decreasing amount of extension (Fig. 1).

5.9 Regional stress field

The tectonic interpretation resolved the nodal plane ambiguity of most moment tensors. We inverted the resultant slip vector orientations for the regional deviatoric unit stress tensor $\hat{S}$ by minimizing the misorientation between the slip vector and the predicted largest shear stress on the fault plane, using the *slick* toolbox (Michael 1984, 1987). In north–east–down-convention:

$$\hat{S} = \begin{pmatrix} -0.798 & 0.596 & -0.004 \\ 0.596 & 0.867 & 0.177 \\ -0.004 & 0.177 & -0.069 \end{pmatrix} \tag{5}$$

The stress tensor indicates near-horizontal, N18°W-oriented compression σ_1, N72°E-oriented extension σ_3 and a 81° SW-plunging σ_2 (Fig. 3). The relative magnitudes of σ_1, σ_2 and σ_3 are –0.99, –0.09 and 1.08. The stress field is dominantly strike-slip with a reverse faulting component. σ_1 is about parallel to the GNSS vectors in the Pamir interior and σ_1 at mantle depth (Bloch *et al*. 2021). σ_2 has a compressional component, represented by the shape factor $\frac{\sigma_2-\sigma_1}{\sigma_3-\sigma_1} = 0.44$, or the compensated linear vector dipole component of the stress tensor of 17 per cent. We interpret the vertical compression component to reflect the bulk thinning of the crust of the Pamir Plateau due to its westward (along the σ_3-orientation) collapse into the Tajik Depression.

5.10 Discussion of seismotectonic processes

Tectonically, the earthquake sequence recorded between August 2015 and July 2017 outlines the first-order deformation field of the Pamir and southernmost Tian Shan. The northward displacement of the eastern Pamir Plateau, tied to the Tarim-Basin lithosphere, is absorbed to a large extent along the Pamir front, the MPTS. Basement-rooted faults of the Palaeozoic Tian Shan orogen, that have been re-activated since ∼12 Ma (e.g. Käßner *et al*. 2016; Abdulhameed *et al*. 2020), most recently yielded during the Sary-Tash (*C*) and Karamyk (*H*) earthquakes on both ends of the Alai Valley, where the MPTS interacts with the Tian Shan. This requires the activation of a basal detachment deeper than that of the MPTS in Jurassic evapourites, that governs the fold-thrust belt of the Tajik Depression (e.g. Bekker 1996; Gagała *et al*. 2020). About E–W extension in the eastern Pamir along the Kongur Shan-Taxkorgan Normal Fault System (*I*), with northward increasing amounts (Robinson *et al*. 2007), is transferred into dextral strike-slip along the Muji Fault and—under increasingly transpressional deformation—via the western Muji Fault and the Kyzilart Transfer Zone into and across the MPTS to the Pamir Frontal Thrust; the latter is characterized by range-front segmentation in thrusts and dextral strike-slip faults (e.g. Arrowsmith & Strecker 1999; Sippl *et al*. 2014).

The Pamir Plateau is dissected by the SKFS into the relative aseismic eastern Pamir block and the western Pamir with higher seismic activity (Schurr *et al*. 2014). Although we concur with the interpretation that the SKFS is part of the broad and distributed zone of sinistral strike-slip faulting along the western margin of the Indian mantle lithosphere indenter (Metzger *et al*. 2017), several aspects of this fault zone are particular: (1) The two largest historical crustal earthquakes of the Pamir interior—the 1911 and 2015 Sarez earthquakes—occurred at the southern end of the SKFS, approximately above the northeastern tip of the indenter (Fig. 1b); (2) the SKFS is morphologically well-expressed along the Sarez, Kokujbel and Karakul segments, but loses expression entering the MPTS and the southwestern Pamir; (3) neotectonically, the northern Kokujbel and Karakul segments show the clearest evidence of ∼E–W extension, suggesting a northward increasing extensional component (from the Sarez to the Karakul segments), akin to that of the Kongur-Shan-Taxkorgan Normal Fault System. We speculate that the SKFS nucleated above the tip of the indenter and has been growing towards the NE and SW. The northward-increasing transtensional component in the Sarez aftershocks, the rift appearance of the Karakul segment, the anticlockwise change in strike of the northernmost SKFS segments, and the (little-studied) merger of these strands with the MPTS (Figs 10b and 4) suggest increasingly stronger westward motion of material from the eastern Pamir in the east to the Tajik Depression to the west, and from the Hindu Kush and Karakorum in the south to the front of the Pamir in the north; this is traced by the GNSS velocity vectors (Fig. 1b; Metzger *et al*. 2020; Zubovich *et al*. 2022) and the anticlockwise rotations recorded in the northern Tajik Depression by palaeomagnetic data (Pozzi & Feinberg 1991; Thomas *et al*. 1994). The SKFS at and south of Lake Sarez and the dextral Aksu-Murghab Fault Zone and its western prolongation, the Sarez-Murghab Thrust System, may outline—on first-order—the triangular shape of the tip of the mantle indenter by distributed deformation in the crust (Figs 1 and 3).

While the eastern Pamir is growing outward into the Tarim basin by thrusting (*F*), the entire western Pamir has a significant component of ∼E–W extension (*D*), reflecting its collapse into the Tajik Depression. The westward increasing extensional component is accommodated by an increase in the dextral strike-slip component along the western MPTS (e.g. the Vakhsh Thrust System; Fig. 1b; Metzger *et al*. 2020), and the involvement of the southern Tian Shan in the Pamir deformation field by thrusting and dextral strike-slip faulting (*H*; for the neotectonic evolution see Käßner *et al*. 2016).

Elliott *et al*. (2020) proposed that the fault zone on which the Khorog earthquake G^* is located as the source of the 1911 Sarez earthquake. The relative seismic quiescence between the Sarez aftershock B^* and the Khorog earthquake G^* (Figs 2a, 3 and S8a) may suggest that the ∼55-km-long fault segment in between was not critically stressed, perhaps due to the occurrence of the 1911 earthquake on the enclosed segment. This length estimate would result in an empirical magnitude of M7.0 (Wells & Coppersmith 1994), which is in approximate agreement with the reported teleseismic body wave magnitude $m_b = 7.3 \pm 0.2$ of the 1911 earthquake (Kulikova *et al*. 2016).

6 FAULT INTERACTION

We argued at the outset that the probability of the three largest earthquakes occurring by chance in such close vicinity in space and time is low. In the present case, transferred stresses acted highly oblique or opposed to the slip directions of the receiving faults (Fig. 7). In the following, we investigate potential aseismic creep using geodetic time-series and test if static Coulomb failure stress changes (ΔCFS) from the consecutive earthquake ruptures are able to explain rupture triggering of the neighbouring faults.

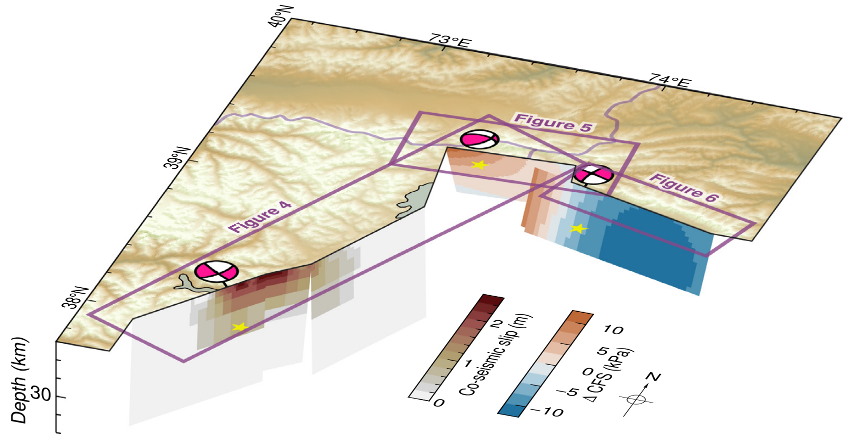

Figure 7. Perspective view onto the three activated fault segments, with slip of the Sarez earthquake (Fig. 4) and thereby imposed static change in Coulomb failure stress (ΔCFS) on the Sary-Tash (Fig. 5) and Muji (Fig. 6) earthquake faults. Stars: earthquake hypocentres. The Coulomb Failure Stress change on the fault planes of the future large earthquakes is small (∼5 kPa) or even negative (∼–7 kPa).

6.1 Methods

6.1.1 InSAR displacement and fault creep model

To investigate the contribution of possible postseismic slip on the SKFS to the regional stress budget, we analysed automatically generated radar interferograms (Lazecký *et al*. 2020) of ascending frame 100A_052 and descending frame 005D_050 (following Comet LiCS naming convention), covering the southern and northern part of the SKFS, respectively. We included all available data following the Sarez main shock, that is 27 months for the southern frame (36 radar scenes, 93 interferograms; Fig. S11), and 5 months for the northern frame (5 radar scenes, 7 interferograms, Fig. S12), before they were affected by the Sary-Tash earthquake. After a visual data inspection and manual unwrapping error correction we calculated linear displacement rates using the small-baseline time-series analysis software *LiCSBAS* (Morishita *et al*. 2020). We subsampled (multilooked) the original interferograms four times to a spatial resolution of ∼400 m, clipped them to the area of interest and subtracted the predicted atmospheric signal delay using state-of-the-art weather models (Yu *et al*. 2018). We applied a temporal low-pass filter of 42 d and a spatial low-pass filter of 2 km to the time-series of frame 100A_052, and no filter to frame 005D_050 (Hooper 2008). Then we extracted linear rate maps (Fig. S13).

We converted the rate maps into displacement accumulated over the 202 d between the Sarez and Sary-Tash main shocks, assuming a constant displacement rate due to post-seismic slip within the first few months following the Sarez main shock. We modelled the observed surface displacements using vertical, rectangular dislocation sources (Okada 1985) with uniform sinistral slip, assuming a homogeneous half-space subsurface model with Lamé's parameters $\lambda = 32$ GPa and $G = 32$ GPa. Source location, depth and amount of slip were modified interactively using *kite* (Isken *et al*. 2017) until the predicted surface displacements fitted our observations reasonably well.

6.1.2 Coulomb stress changes

We modelled to which extent the stresses induced by the large earthquakes and corresponding foreshocks loaded or unloaded nearby fault segments by computing the change in Coulomb failure stress ΔCFS (Harris 1998):

$$\Delta\mathrm{CFS} = \Delta\tau + \mu(\Delta\sigma_n + \Delta p). \tag{6}$$

$\Delta\tau$ is the change in shear stress on the fault (positive in slip direction), and $\Delta\sigma_n$ is the change in normal stress (a positive ΔCFS acts destabilizing). For most rocks μ is between 0.6 and 0.8 (Harris 1998). Under the assumption of undrained conditions (pore fluids do not escape or enter the fault), Δp is proportional to the mean stress change inside the fault (Rice & Cleary 1976):

$$\Delta p = -\beta\frac{\Delta\sigma_{kk}}{3}, \tag{7}$$

where $\Delta\sigma_{kk}$ is the sum of the diagonal elements of the stress tensor and β is the Skempton coefficient. β lies between 0.5 and 1.0 for rocks, but is typically between 0.7 and 0.9 (Harris 1998; Cocco & Rice 2002). β and μ are often combined into the apparent friction coefficient:

$$\mu' = \mu(1-\beta). \tag{8}$$

We modelled the stress changes in response to the largest earthquakes, foreshocks and post-seismic slip transients using *pscmp* (Wang *et al*. 2006). We constructed dislocation sources (Okada 1985) from published fault-slip models (He *et al*. 2018; Metzger *et al*. 2017; Bie *et al*. 2018) and our own earthquake moment tensors. The fault length l and width w of moment tensor sources were estimated from M_W using the empirical scaling relationships of Wells & Coppersmith (1994):

$$l = 10^{(M_\mathrm{W}-4.38)/1.49} \tag{9}$$

$$w = 10^{(M_\mathrm{W}-4.06)/2.25}. \tag{10}$$

Slip s was calculated from $M_0 = AGs$, with the seismic moment M_0, fault area A, and shear modulus $G = 32$ GPa. The slip sense was determined after resolution of the nodal plane ambiguity (Section 4). We then computed ΔCFS according to eqs (6) and (7) at the origin times and on the fault planes of the three large earthquakes and significant foreshocks. We used an elastic half-space subsurface model with Lamé's parameters $\lambda = 32$ GPa and $G = 32$ GPa and chose $\mu = 0.8$ and $\beta = 0.75$, so that the earthquake hypocentres received the largest ΔCFS concentration while the parameters remained in the physically plausible range. We tested $\mu = 0.4$ and $\beta = 0.5$ as well as the debated assumption that $\Delta p = 0$ (Harris 1998) by letting

$\beta = 0$ and $\mu = \mu' = 0.2$ (Figs S14 and S15). We found uncertainties in ΔCFS by randomly perturbing the modelling parameters using a normal distribution. The half-space parameters λ and G were varied with a standard deviation of 5 GPa; the fault properties μ and β with one of 0.2 (assuring they remained in the [0, 1] range); and the fault's strike, dip and rake with one of 5°. We report the median, and the 5 and 95 per cent quantiles of the resulting distributions (Table 1, Figs S16 and S17).

6.2 Post-seismic creep on the Sarez-Karakul Fault System

The accumulated InSAR line-of-sight displacements between the Sarez and the Sary-Tash main shocks show a distinct change along the mapped SKFS (Fig. 8a). While the data base of the southern frame is dense enough to provide a good signal-to-noise ratio in the time-series for detecting tectonic signals, the resulting rates in the northern frame—based on 5 radar scenes—may be dominated by local atmospheric conditions (Fig. S13).

The southern frame highlights sinistral motion and uplift east of the SKFS of ∼8 mm in the look direction between the first satellite pass on 30 December 2015 and the Sary-Tash earthquake (Fig. 8a; Jin *et al*. 2022). The sinistral motion agrees with the coseismic slip model of Metzger *et al*. (2017); the displacement amplitude is reasonable as well (∼1 per cent of the coseismic slip; Metzger *et al*. 2017), given that our observations do not capture the first 3 weeks of the post-seismic slip history.

In the northern frame, earthquake focal mechanisms indicate sinistral slip along the SKFS-segments north of Lake Karakul (Fig. 4a; see also Schurr *et al*. 2014). Even though the view direction is nearly insensitive to lateral slip, we assume—due to the significant across-strike displacement changes, the along-strike correlation of the signal, the seismic activity along the fault segments, and the location of events *c'* and C^* close to the northern tip of the SKFS—that the displacement signal is due to post-seismic creep on the SKFS; this allows to test whether creep may have contributed to the triggering of the Sary-Tash earthquake. The positive sign west of the SKFS (the ground moved towards the satellite) indicates that the signal is not due to a normal faulting component.

We modelled our displacement observations as aseismic slip on seven vertical fault patches between 0.5 and 10.5 km depth along two segments of the SKFS between the epicentres of the Sarez and the Sary-Tash earthquakes (Kokujbel segment in the south, Karakul segment in the north; Figs 4d and 8b). Our model indicates a maximum cumulative creep between 20 and 30 mm in the 202 d between the earthquakes on the Kokujbel segment (∼35–55 mm yr^{-1}, Fig. S13), which occupies part of the slip patch of the Sarez earthquake. On the Karakul segment, we find a total maximum displacement of 40 mm (∼72 mm yr^{-1}) in the south to 25 mm (∼45 mm yr^{-1}, Fig. S13) in the north. The segment links the coseismically active part of the SKFS with the Kyzilart Transfer Zone, which connects the Muji Fault with the Pamir Frontal Thrust (Figs 5a and 8a; Sippl *et al*. 2014).

6.3 Static Coulomb stress changes

The Sarez earthquake caused a long-wavelength positive ΔCFS on the Sary-Tash earthquake fault (Fig. 5g) with the highest values in the shallowest and westernmost part. It loaded the rupture plane, foreshock *c'*, and hypocentre C^* only weakly (∼4 kPa; Table 1). Creep on the SKFS (Fig. 8) may have additionally loaded the Sary-Tash earthquake fault, mainly in the upper westernmost part, and with a lobe of increased ΔCFS that reaches towards the hypocentre at ∼10 km depth (Fig. 5g). East of the hypocentre, the foreshock *c'* loaded the rim of the rupture plane. Together they caused a ΔCFS concentration of 4^{+4}_{-3} kPa at the hypocentre (Table 1; Fig. S15). Even with favourable (low-β) fault parameters, ΔCFS at the Sary-Tash hypocentre does not exceed 10 kPa (Fig. S14; see also Jin *et al*. 2022). These values may be just above the tidal shear stresses that the dip-slip fault experiences over the course of a day (∼5 kPa; Tanaka *et al*. 2002). An additional ΔCFS contribution may be caused by viscous relaxation of the lower crust in the months following the Sarez earthquake, which would constitute an additional, deeper source with the same sense of motion and therefore a comparable effect as the earthquake itself. Static stress change induced by the 2008 Nura earthquake loaded the fault in the order of ∼1 MPa (Fig. S14). Despite this large stress perturbation, the Sary-Tash earthquake did not rupture before 2016. The area with the highest ΔCFS change west of the hypocentre did not rupture in an earthquake and did not produce many aftershocks (Figs 5e–f). It might be that the MPTS in this part—close to the intersection with the SKFS—has a different orientation than modelled; ΔCFS may therefore be smaller or even negative. It is also possible that the MPTS was not critically stressed, for example because it ruptured in an earlier unrecorded earthquake. Lastly, the fault properties of the adjacent segment may be such that it slips aseismically.

The ΔCFS model for the Muji earthquake (Fig. 6d) suggests that the Sarez and Sary-Tash earthquakes unloaded the fault plane with a total negative ΔCFS of -19^{+7}_{-6} kPa (Figs S15 and S17; Table 1). For the Sarez earthquake, the effect is mostly due to clamping of the Muji fault through normal stress and a slight loading opposite to the slip sense, that is relaxation. The Sary-Tash earthquake imposed sinistral strain on the Muji fault, as it pulled the northern wall towards the northwest relative to the southern wall; this is opposite to the dextral slip of the earthquake. The 2008 Nura earthquakes also imposed sinistral slip on the Muji fault. The foreshock *e'* stressed the hypocentre with ΔCFS ≈ 60 kPa. However, the remainder of the fault plane stayed in an unloaded and clamped state. As the foreshock had a focal mechanism and location almost identical to the main shock, our model can neither explain triggering of the forehsock *e'* through CFS changes. We conclude that static stress changes counteracted the pending Muji rupture occurred due to another trigger.

Static stress changes are a viable trigger for the moderate earthquakes in the southern (e.g. events B^*, G^*, Table 1) and northern continuation of the SKFS (e.g. events *2*, *4*, *28*; Table 1; Fig. 3), as well as all aftershocks of the Sary-Tash and Muji earthquakes (sequences *C* and *E* in Table 1). Our model indicates positive ΔCFS, typically between 10s and 100s kPa for these events. Similar stress magnitudes have been found for the aftershocks in the near-field (within about one rupture length) of many large earthquakes (Toda *et al*. 1998; Stein 1999; Parsons & Dreger 2000; Sippl *et al*. 2014; Wiseman & Burgmann 2011). We consider negative ΔCFS values in the near-field of the large main shocks as artefacts of the too coarse fault-slip models that lack small scale slip heterogeneities. The slip models therefore wrongly predict slip (and hence negative ΔCFS values) in places where aftershocks indicate stressed remnants in or near the rupture plane. Earthquakes located at large distances from any large earthquakes (>100 km; F^*, H^*, I^*) received no more than a miniscule ΔCFS and may have occurred independently of the large main shocks.

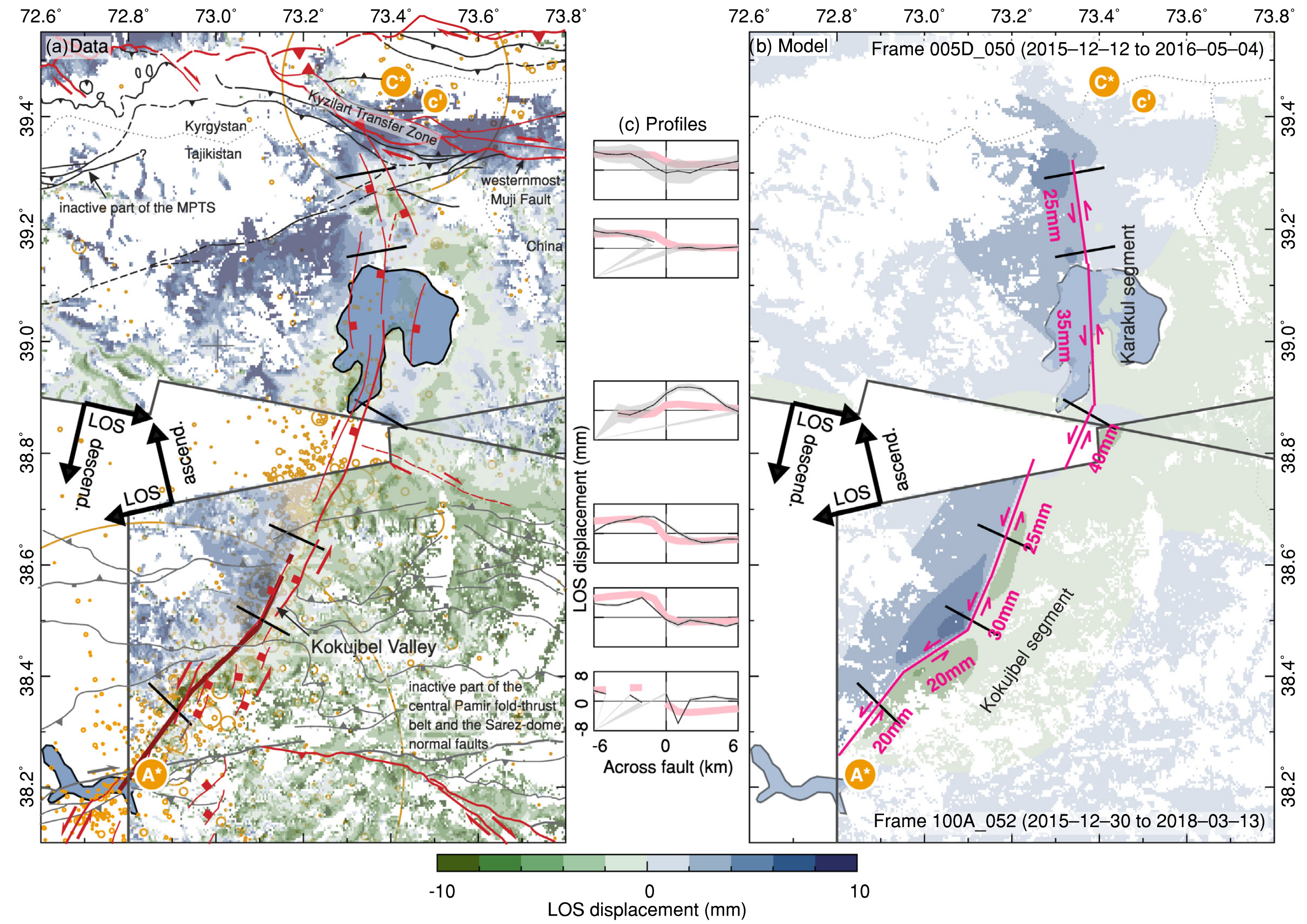

Figure 8. Post-seismic displacement on the Sarez-Karakul Fault System. (a) InSAR displacement map derived from the displacement-rate map (Fig. S12). Seismicity between A^* and C^*, main shock and foreshock hypocentres highlighted in orange. Mapped Cenozoic structures in grey and neotectonic structures in red. (b) Fault creep model and synthetic data. (c) Across-strike displacement profiles with data (black), nominal data uncertainty (grey) and model (pink). Displacement is accumulated in 202 d between events A^* and C^*. LOS: line-of-sight vector. See Fig. 4(d) for along-strike view of the creep model and Fig. S12 for uncertainty in map view.

6.4 Discussion of fault interaction

The characteristics of the 2015–2017 Pamir earthquake sequence differ from the sequences in the central Apennines (e.g. Chiaraluce *et al*. 2017), Baluchistan (Yadav *et al*. 2012), southern California (e.g. Hauksson *et al*. 1993; Parsons & Dreger 2000) and South Iceland (e.g. Hreinsdóttir *et al*. 2009) in that in the Pamir, faults interacted over much larger distances ($\geq$100 km, compared to $\leq$30 km) and on kinematically dissimilar faults. In terms of duration, the sequences in Baluchistan and South Iceland came to rest within only a few months (Árnadóttir *et al*. 2003; Hreinsdóttir *et al*. 2009; Yadav *et al*. 2012), whereas the Sunda Arc (e.g. Wiseman & Burgmann 2011) and Southern California (e.g. Parsons & Dreger 2000) experienced recurring seismic activity within 7 yr, and the southern Apennines within almost 10 yr (e.g. Chiaraluce *et al*. 2017). The three $M_W > 6.4$ earthquakes of the present sequence ocurred within a year and no $M_W > 5.5$ in the 5 yr after.

The Sary-Tash earthquake—that motivated this study—and its foreshock *c'*, may have received a ΔCFS as low as 4 kPa, even if post-seismic slip on the SKFS is considered. In case of the Muji earthquake, negative ΔCFS values indicate stabilization of the rupture plane and foreshock *e'* hypocentre, which suggests that it ruptured *despite of*—not due to—the static stress changes imposed by the previous earthquakes. We cannot exclude that the complexity of the Sary-Tash earthquake, indicated by the diverse aftershock mechanisms, may have caused a more complex deformation pattern below the MPTS, but we consider it unlikely that it reversed the modelled stress relaxation. The consistency between the large earthquake moment tensors and the regional stress tensor (Fig. 3) implies that the earthquakes responded to the long-term tectonic loading. That foreshock activity is at most weakly dependent on previous main shock occurrence (Fig. 2) corroborates the inference that the static stress changes contributed only little to the total stress budget of the faults. There is some indication that faults that are oriented closer to perpendicular to σ_1 show a faster decay of the aftershock rate, manifest in a higher Omori-Utsu *p*-value (Fig. S18). This may indicate a faster healing of the fault gauge through tectonic stresses when the fault is favourably oriented with respect to the ambient stress (Miller 2020).

Low ($\sim$10kPa) or negative ΔCFS values are regularly reported for subsequent earthquakes in a sequence (e.g. Perfettini *et al*. 1999; Parsons & Dreger 2000; Ziv & Rubin 2000; Hardebeck *et al*. 1998; Wiseman & Burgmann 2011; DeVries *et al*. 2018). Discrepancies between stress transfer models and actual earthquake occurrence could in some cases be ascribed to insufficient account for historic earthquakes (Mildon *et al*. 2017, 2019) or the predominant contribution of secular tectonic loading to earthquake occurrence

(Toda *et al*. 1998; Mildon *et al*. 2017). To reconcile the timing of aftershocks, deliberately adjusted rate- and state-dependent fault friction parameters may be required (Dieterich 1994), which implies accelerating pre-slip on the fault (Dieterich 1992). In the present sequence, foreshocks indeed do show a tendency to surround the future rupture plane and approach the future hypocentre (Ellsworth & Bulut 2018; Schurr *et al*. 2020), but foreshock rate barley exceeded background rate (Sippl *et al*. 2013b; Schurr *et al*. 2014) and was not accelerating on any fault (Fig. 2c). Viscous processes have been suggested for the delayed triggering of the 1999 Hector Mine by the 1992 Landers earthquake (Hauksson *et al*. 1993). Post-seismic models of the Sarez earthquake, however, suggest that viscoelastic relaxation can be neglected (Jin *et al*. 2022). Beyond the near-field, dynamic stress changes probably play an important role to generate aftershocks (Felzer & Brodsky 2006) or even trigger remote earthquakes (Gomberg & Johnson 2005). But dynamic stresses act immediately (e.g. Shimojo *et al*. 2021) or with a delay of no more than hours (Peña Castro *et al*. 2019) and do not provide an explanation for the multimonth delays between the events.

7 FLUID PROCESSES

That the observed seismicity, that is the three major sequences but also the moderate ones, occurred at with time increasing distances from the Sarez earthquake rupture that mimic a diffusion law (Fig. 2e, eq. 3, Video 1), may point at a contribution of fluid migration to the earthquake triggering. Pore pressure counteracts normal stress and has a decisive effect on the frictional stability of faults. Faults are hydrological systems that store fluids if sealed and guide them if permeable. In sealed fault systems, fluids may be pressurized. An earthquake may breach seals and mobilize fluids (Sibson 1992; Brodsky 2003). Brittle damage generated by main shock and aftershocks can increase the permeability of a fault zone by orders of magnitude (Kitagawa *et al*. 2002; Miller & Nur 2000), particularly in the damage zone surrounding the fault core, creating pathways for fluids (Miller 2020). There is geophysical evidence for fluids in Pamir's upper crust that contains the fault systems discussed here: a magneto-telluric profile—traversing the Pamir near the Sary-Tash earthquake—showed high-conductivity regions across the MPTS that were interpreted as due to aqueous fluids within the damage zones (Sass *et al*. 2014). This is corroborated by significantly increased *P*- to *S*-wave velocity ratios in the upper ∼10 km of the crust along the MPTS detected by tomography (Sippl *et al*. 2013a). A contribution of poro-elastic rebound is consistent with the post-seismic deformation pattern of the Sarez earthquake (Jin *et al*. 2022). The fault zones that ruptured during the three major earthquakes are almost adjoining and likely interconnected. We hypothesize that fluids captured in the fault zone of the Sarez earthquake were coseismically freed and pressured along the SKFS, where permeability may have been increased by brittle fracturing and transient stress changes (Fitzenz & Miller 2001; Manga *et al*. 2012), generating relatively distant and delayed aftershocks, reaching the MPTS and triggering the Sary-Tash earthquake. Coseismically activated thermal decomposition of the Devonian basement carbonates (Section 5.2) may have contributed an additional fluid source (Han *et al*. 2007; Gunatilake & Miller 2022) that could account for the three times higher aftershock productivity (*K* in eq. 4) of this earthquake compared to the similarly sized Muji earthquake (Fig. S9). The Sary-Tash earthquake may have initiated another fluid pressure wave sweeping through the fracture mesh connecting the MPTS and the Muji fault zone, eventually triggering the third event. Fluid triggering of the Muji earthquake may also account for the near-simultaneous rupture of both slip patches (Bie *et al*. 2018). The swarm-like normal faulting sequence *D*, overlapping with the Sarez earthquake sequence, may have been initiated by dynamic perturbation of the hydraulic system through transient stresses from strong shaking, as has frequently been observed (Manga *et al*. 2012; Shimojo *et al*. 2021). The progression of a fluid front with time may be described by the square-root envelope-function of eq. (3). Seismic event clouds that expand according to such a relationship are regularly observed in controlled fluid injection scenarios, such as hydrologically fracturing geothermal reservoirs (Shapiro *et al*. 2003; Ogwari & Horton 2016). For seismicity north of the Sarez earthquake, the hydraulic diffusivity *D* can be estimated to the first order between 30 and 40 $m^2\,s^{-1}$; south of the earthquake between 12 and 20 $m^2\,s^{-1}$ (Fig. 2e). It must be kept in mind that the genuine diffusivity of the system is likely anisotropic and variable in space and time (Shapiro *et al*. 2003; Ross *et al*. 2020). Our estimates are stable with respect to the choice in origin (Fig. S8). Setting a new origin at the eastern end of the Sary-Tash earthquake for the later sweep to the Muji earthquake results in the same values. $D \approx$ 12–40 $m^2\,s^{-1}$ is well within the range suggested by Shapiro *et al*. (2003) of 10^{-2} to 10^{-1} $m^2\,s^{-1}$ for crystalline rocks to 10^2 $m^2\,s^{-1}$ for a recently ruptured subduction megathrust fault. Observations of shaking induced swarm activity similarly indicates *D* in the order of 25–100 $m^2\,s^{-1}$ (Shimojo *et al*. 2021).

8 CONCLUSION

We analysed the seismic record of the earthquake sequence that struck the Pamir highlands in 2015–2017. Our observation started ∼4 months before the initial M_W 7.2 Sarez earthquake, for which no significant precursory seismic activity could be detected. The subsequent M_W 6.4 Sary-Tash and M_W 6.6 Muji earthquakes on adjacent faults, but more than 80 km away, showed foreshock activity, as did other M_W 4.4–5.7 earthquakes in the region. The aftershock seismicity traced the activated fault zones and testifies to the Pamir Plateau dissecting nature of the Sarez Karakul Fault System, interaction of the Main Pamir Thrust System with the northerly adjacent Tian Shan, and growth of the Pamir over the Tarim Basin in the east. The 1911 Sarez earthquake likely occurred on the fault segment enclosed by the M_W 5.3 Sarez aftershock and the M_W 4.9 Khorog earthquakes. Static stress transfer from the main shocks, post-seismic deformation and moderate foreshocks contributed at most subordinately to the stress budget of the activated fault segments. More likely, fluids migrated through the damaged fault zones and triggered the subsequent earthquakes. An improved detection and quantification of such fluid processes is required to gain a better understanding of the mechanisms that trigger seismicity during periods of seismic unrest.

ACKNOWLEDGMENTS

We thank the drivers and field participants from the Institute of Tibetan Plateau Research, especially Hongbing Liu, who helped to organize the station deployment; Christian Sippl, Sebastian Hainzl and Rongjiang Wang for sharing code and discussion; Serge A. Shapiro for discussion; Chris Chafe for introducing data sonification; Ayleen Gaete for assisting the data processing; Stephen Miller, Bogdan Enescu and two anonymous reviewers for their constructive comments on the manuscript. Funded by the CaTeNA project of the German Federal Ministry of Science and Education (support codes 03G0878A and 03G0878B) and German Research Council project RA 442/41 and BL 1758/1-1. Open Access facilitated through project DEAL. Seismic data were handled using *obspy* (Krischer *et al*. 2015) and *pyrocko* (Heimann *et al*. 2017). Figures were created with the help of the *Generic Mapping Tools* (Wessel *et al*. 2013), *maplotlib* (Hunter 2007) and *Scientific Color Maps* (Crameri *et al*. 2020). Part of the instruments were provided by GIPP of GFZ Potsdam.

DATA AVAILABILITY

Seismic data are archived in the GEOFON data centre (Yuan *et al*. 2018a, b). The seismic event and moment tensor catalogs are available through GFZ data services (Bloch *et al*. 2022). InSAR data were downloaded from LiCSAR (Looking into the Continents from Space), which contains modified Copernicus Sentinel data analysed by the Centre for the Observation and Modelling of Earthquakes, Volcanoes and Tectonics (COMET; https://comet.nerc.ac.uk/comet-lics-portal). LiCSAR uses JASMIN, the UK's collaborative data analysis environment.

REFERENCES

Abdulhameed, S. *et al.*, 2020. Tajik basin and southwestern Tian Shan, northwestern India-Asia collision zone: 2. Timing of basin inversion, Tian Shan mountain building, and relation to Pamir-plateau advance and deep India-Asia indentation, *Tectonics,* **39**(5), e2019TC005873, doi:10.1029/2019TC005873.

Aldersons, F., 2004. Toward three-dimensional crustal structure of the Dead Sea region from local earthquake tomography, *PhD thesis*, Tel-Aviv University, Tel Aviv, Israel.

Árnadóttir, T., Jónsson, S., Pedersen, R. & Gudmundsson, G.B., 2003. Coulomb stress changes in the South Iceland Seismic Zone due to two large earthquakes in June 2000, *Geophys. Res. Lett.,* **30**(5), doi:10.1029/2002GL016495.

Arrowsmith, J.R. & Strecker, M., 1999. Seismotectonic range-front segmentation and mountain-belt growth in the Pamir-Alai region, Kyrgyzstan (India-Eurasia collision zone), *Bull. geol. Soc. Am.,* **111**(11), 1665–1683.

Bekker, Y.A., 1996. Tectonics of the Afghan-Tajik depression, *Geotectonics,* **30**(1), 64–70.

Bie, L., Hicks, S., Garth, T., Gonzalez, P. & Rietbrock, A., 2018. 'Two go together': near-simultaneous moment release of two asperities during the 2016 Mw 6.6 Muji, China earthquake, *Earth planet. Sci. Lett.,* **491,** 34–42.

Bloch, W., Schurr, B., Yuan, X., Ratschbacher, L., Reuter, S., Kufner, S.-K., Xu, Q. & Zhao, J., 2021. Structure and stress field of the lithosphere between Pamir and Tarim, *Geophys. Res. Lett.,* **48**(22), e2021GL095413, doi:10.1029/2021GL095413.

Bloch, W., Schurr, B., Yuan, X., Xu, Q., Zhao, J., Murodkulov, S. & Oimuhammadzoda, I., 2022. Earthquake and Moment Tensor Catalogs of the 2015-2017 Pamir Earthquake Sequence. GFZ Data Services. doi:10.5880/fidgeo.2022.007.

Bondár, I., Engdahl, E.R., Villaseñor, A., Harris, J. & Storchak, D., 2015. ISC-GEM: global instrumental earthquake catalogue (1900–2009), II. location and seismicity patterns, *Phys. Earth planet. Inter.,* **239,** 2–13.

Bormann, P. & Dewey, J.W., 2012. The new IASPEI standards for determining magnitudes from digital data and their relation to classical magnitudes, *New Manual of Seismological Observatory Practice 2 (NMSOP-2),* pp. 1–44, Deutsches GeoForschungsZentrum GFZ.

Bouchon, M., 1981. A simple method to calculate Green's functions for elastic layered media, *Bull. seism. Soc. Am.,* **71**(4), 959–971.

Briggs, R.W. *et al.*, 2006. Deformation and slip along the Sunda megathrust in the great 2005 Nias-Simeulue earthquake, *Science,* **311**(5769), 1897–1901.

Brodsky, E.E., 2003. A mechanism for sustained groundwater pressure changes induced by distant earthquakes, *J. geophys. Res.,* **108**(B8), doi:10.1029/2002JB002321.

Burtman, V.S. & Molnar, P.H., 1993. *Geological and Geophysical Evidence for Deep Subduction of Continental Crust Beneath the Pamir,* Vol. **281,** Geological Society of America.

Chen, K., Avouac, J.-P., Aati, S., Milliner, C., Zheng, F. & Shi, C., 2020. Cascading and pulse-like ruptures during the 2019 Ridgecrest earthquakes in the Eastern California Shear Zone, *Nat. Commun.,* **11**(1), 1–8.

Chevalier, M.-L., Pan, J., Li, H., Liu, D. & Wang, M., 2015. Quantification of both normal and right-lateral late Quaternary activity along the Kongur Shan extensional system, Chinese Pamir, *Terra Nova,* **27**(5), 379–391.

Chiaraluce, L., Ellsworth, W., Chiarabba, C. & Cocco, M., 2003. Imaging the complexity of an active normal fault system: The 1997 Colfiorito (central Italy) case study, *J. geophys. Res.,* **108**(B6), doi:10.1029/2002JB002166.

Chiaraluce, L. *et al.*, 2017. The 2016 Central Italy seismic sequence: a first look at the mainshocks, aftershocks, and source models, *Seismol. Res. Lett.,* **88**(3), 757–771.

Cocco, M. & Rice, J.R., 2002. Pore pressure and poroelasticity effects in coulomb stress analysis of earthquake interactions, *J. geophys. Res.,* **107**(B2), ESE 2–1-ESE-17.

Comino, J. Á.L., Heimann, S., Cesca, S., Milkereit, C., Dahm, T. & Zang, A., 2017. Automated full waveform detection and location algorithm of acoustic emissions from hydraulic fracturing experiment, *Proc. Eng.,* **191,** 697–702.

Cowgill, E., 2009. Cenozoic right-slip faulting along the eastern margin of the Pamir salient, northwestern China, *Bull. geol. Soc. Am.,* **122**(1-2), 145–161.

Crameri, F., Shephard, G.E. & Heron, P.J., 2020. The misuse of colour in science communication, *Nat. Commun.,* **11**(1), 1–10.

Das, S. & Henry, C., 2003. Spatial relation between main earthquake slip and its aftershock distribution, *Rev. Geophys.,* **41**(3), doi:10.1029/2002RG000119.

DeVries, P. M.R., Viégas, F., Wattenberg, M. & Meade, B.J., 2018. Deep learning of aftershock patterns following large earthquakes, *Nature,* **560**(7720), 632–634.

Di Giacomo, D., Engdahl, E.R. & Storchak, D.A., 2018. The ISC-GEM earthquake catalogue (1904–2014): status after the extension project, *Earth Syst. Sci. Data,* **10**(4), 1877–1899.

Diehl, T., Deichmann, N., Kissling, E. & Husen, S., 2009. Automatic S-wave picker for local earthquake tomography, *Bull. seism. Soc. Am.,* **99**(3), 1906–1920.

Dieterich, J.H., 1992. Earthquake nucleation on faults with rate-and state-dependent strength, *Tectonophysics,* **211**(1–4), 115–134.

Dieterich, J.H., 1994. A constitutive law for rate of earthquake production and its application to earthquake clustering, *J. geophys. Res.,* **99**(B2), 2601–2618.

Einarsson, P., Björnsson, S., Foulger, G., Stefánsson, R. & Skaftadóttir, T., 1981. Seismicity pattern in the South Iceland Seismic Zone, in *Maurice Ewing Series,* pp. 141–151, American Geophysical Union.

Elliott, A., Elliott, J., Hollingsworth, J., Kulikova, G., Parsons, B. & Walker, R., 2020. Satellite imaging of the 2015 M 7.2 earthquake in the Central Pamir, Tajikistan, elucidates a sequence of shallow strike-slip ruptures of the Sarez-Karakul fault, *Geophys. J. Int.,* **221**(3), 1696–1718.

Ellsworth, W.L. & Bulut, F., 2018. Nucleation of the 1999 Izmit earthquake by a triggered cascade of foreshocks, *Nat. Geosci.,* **11**(7), 531–535.

Ellsworth, W.L., Giardini, D., Townend, J., Ge, S. & Shimamoto, T., 2019. Triggering of the Pohang, Korea, Earthquake (Mw 5.5) by enhanced geothermal system stimulation, *Seismol. Res. Lett.,* **90**(5), 1844–1858.

Fan, G., Ni, J.F. & Wallace, T.C., 1994. Active tectonics of the Pamirs and Karakorum, *J. geophys. Res.,* **99**(B4), 7131–7160.

Felzer, K.R. & Brodsky, E.E., 2006. Decay of aftershock density with distance indicates triggering by dynamic stress, *Nature,* **441**(7094), 735–738.

Fitzenz, D.D. & Miller, S.A., 2001. A forward model for earthquake generation on interacting faults including tectonics, fluids, and stress transfer, *J. geophys. Res.,* **106**(B11), 26 689–26 706.

Freed, A.M. & Lin, J., 2001. Delayed triggering of the 1999 Hector Mine earthquake by viscoelastic stress transfer, *Nature,* **411**(6834), 180–183.

Gagała, Ł. *et al.*, 2020. Tajik Basin and Southwestern Tian Shan, Northwestern India-Asia Collision Zone: 1. Structure, kinematics, and salt tectonics in the Tajik Fold-and-thrust belt of the Western Foreland of the Pamir, *Tectonics,* **39**(5), e2019TC005871, doi:10.1029/2019TC005871.

Gomberg, J. & Johnson, P., 2005. Dynamic triggering of earthquakes, *Nature,* **437**(7060), 830–830.

Gunatilake, T. & Miller, S.A., 2022. Spatio-temporal complexity of aftershocks in the Apennines controlled by permeability dynamics and decarbonization, *J. geophys. Res.,* **127**(6), e2022JB024154, doi:10.1029/2022JB024154.

Hamling, I.J. & Upton, P., 2018. Observations of aseismic slip driven by fluid pressure following the 2016 Kaikōura, New Zealand, earthquake, *Geophys. Res. Lett.,* **45**(20), 11030–11039.

Han, R., Shimamoto, T., Hirose, T., Ree, J. & Ando, J., 2007. Ultralow friction of carbonate faults caused by thermal decomposition, *Science,* **316**(5826), 878–881.

Hardebeck, J.L., Nazareth, J.J. & Hauksson, E., 1998. The static stress change triggering model: Constraints from two southern California aftershock sequences, *J. geophys. Res.,* **103**(B10), 24 427–24 437.

Harris, R.A., 1998. Introduction to special section: stress triggers, stress shadows, and implications for seismic hazard, *J. geophys. Res.,* **103**(B10), 24 347–24 358.

Hauksson, E., Jones, L.M., Hutton, K. & Eberhart-Phillips, D., 1993. The 1992 Landers earthquake sequence: seismological observations, *J. geophys. Res.,* **98**(B11), 19 835–19 858.

He, P., Hetland, E.A., Niemi, N.A., Wang, Q., Wen, Y. & Ding, K., 2018. The 2016 Mw 6.5 Nura earthquake in the Trans Alai range, northern Pamir: possible rupture on a back-thrust fault constrained by Sentinel-1A radar interferometry, *Tectonophysics,* **749,** 62–71.

Heimann, S. *et al.*, 2017. Pyrocko - an open-source seismology toolbox and library. GFZ Data Services. doi:10.5880/GFZ.2.1.2017.001.

Hooper, A., 2008. A multi-temporal InSAR method incorporating both persistent scatterer and small baseline approaches, *Geophys. Res. Lett.,* **35**(16), doi:10.1029/2008GL034654.

Hreinsdóttir, S., Árnadóttir, T., Decriem, J., Geirsson, H., Tryggvason, A., Bennett, R.A. & LaFemina, P., 2009. A complex earthquake sequence captured by the continuous GPS network in SW Iceland, *Geophys. Res. Lett.,* **36**(12), doi:10.1029/2009GL038391.

Hunter, J.D., 2007. Matplotlib: a 2D graphics environment, *Comput. Sci. Eng.,* **9**(3), 90–95.

ISC, 2021. ISC-GEM Earthquake Catalogue, Tech. rep., International Seismological Centre.

Ischuk, A. *et al.*, 2013. Kinematics of the Pamir and Hindu Kush regions from GPS geodesy, *J. geophys. Res.,* **118**(5), 2408–2416.

Isken, M., Sudhaus, H., Heimann, S., Steinberg, A., Daout, S. & Vasyura-Bathke, H., 2017. Kite - Software for Rapid Earthquake Source Optimisation from InSAR Surface Displacement. V. 0.1. GFZ Data Services. doi:10.5880/GFZ.2.1.2017.002.

Jade, S. *et al.*, 2004. GPS measurements from the Ladakh Himalaya, India: preliminary tests of plate-like or continuous deformation in Tibet, *Bull. geol. Soc. Am.,* **116**(11–12), 1385–1391.

Jin, Z., Fialko, Y., Zubovich, A. & Schöne, T., 2022. Lithospheric deformation due to the 2015 M7.2 Sarez (Pamir) earthquake constrained by 5 years of space geodetic observations, *J. geophys. Res.,* **127**(4), e2021JB022461, doi:10.1029/2021JB022461.

Käßner, A. *et al.*, 2016. Cenozoic intracontinental deformation and exhumation at the northwestern tip of the India-Asia collision-southwestern Tian Shan, Tajikistan, and Kyrgyzstan, *Tectonics,* **35**(9), 2171–2194.

Kato, A., Fukuda, J., Nakagawa, S. & Obara, K., 2016. Foreshock migration preceding the 2016 Mw 7.0 Kumamoto earthquake, Japan, *Geophys. Res. Lett.,* **43**(17), 8945–8953.

Kissling, E., Ellsworth, W., Eberhart-Phillips, D. & Kradolfer, U., 1994. Initial reference models in local earthquake tomography, *J. geophys. Res.,* **99**(B10), 19 635–19 646.

Kitagawa, Y., Fujimori, K. & Koizumi, N., 2002. Temporal change in permeability of the rock estimated from repeated water injection experiments near the Nojima fault in Awaji Island, Japan, *Geophys. Res. Lett.,* **29**(10), 121-1-121-4.

Kreemer, C., Blewitt, G. & Klein, E.C., 2014. A geodetic plate motion and global strain rate model, *Geochem. Geophys. Geosyst.,* **15**(10), 3849–3889.

Krischer, L., Megies, T., Barsch, R., Beyreuther, M., Lecocq, T., Caudron, C. & Wassermann, J., 2015. ObsPy: a bridge for seismology into the scientific Python ecosystem, *Comput. Sci. Discov.,* **8**(1), doi:10.1088/1749-4699/8/1/014003.

Kufner, S.-K. *et al.*, 2016. Deep India meets deep Asia: lithospheric indentation, delamination and break-off under Pamir and Hindu Kush (Central Asia), *Earth planet. Sci. Lett.,* **435,** 171–184.

Kufner, S.-K., Schurr, B., Haberland, C., Zhang, Y., Saul, J., Ischuk, A. & Oimahmadov, I., 2017. Zooming into the Hindu Kush slab break-off: a rare glimpse on the terminal stage of subduction, *Earth planet. Sci. Lett.,* **461,** 127–140.

Kufner, S.-K., Schurr, B., Ratschbacher, L., Murodkulov, S., Abdulhameed, S., Ischuk, A., Metzger, S. & Kakar, N., 2018. Seismotectonics of the Tajik basin and surrounding mountain ranges, *Tectonics,* **37**(8), 2404–2424.

Kufner, S.-K. *et al.*, 2021. The Hindu Kush slab break-off as revealed by deep structure and crustal deformation, *Nat. Commun.,* **12**(1), 1–11.

Kulikova, G., Schurr, B., Krüger, F., Brzoska, E. & Heimann, S., 2016. Source parameters of the Sarez-Pamir earthquake of 1911 February 18, *Geophys. J. Int.,* **205**(2), 1086–1098.

Langston, C.A. & Dermengian, J.M., 1981. Comment on 'seismotectonic aspects of the Markansu Valley, Tadjikstan, earthquake of August 11, 1974' by James Jackson, Peter Molnar, Howard Patton, and Thomas Fitch, *J. geophys. Res.,* **86**(B2), 1091–1093.

Lazecký, M. *et al.*, 2020. Licsar: an automatic InSAR tool for measuring and monitoring tectonic and volcanic activity, *Remote Sens.,* **12**(15), doi:10.3390/rs12152430.

Lee, W. H.K. & Lahr, J.C., 1972. HYPO71: a computer program for determining hypocenter, magnitude, and first motion pattern of local earthquakes, Open-File Report 72-224, U.S. Geological Survey.

Li, J. *et al.*, 2018. Rupture characteristics of the 25 November 2016 Aketao earthquake (Mw 6.6) in eastern Pamir revealed by GPS and teleseismic data, *Pure appl. Geophys.,* **175**(2), 573–585.

Li, T. *et al.*, 2019. Cumulative and coseismic (during the 2016 Mw 6.6 Aketao Earthquake) deformation of the dextral-slip Muji Fault, Northeastern Pamir Orogen, *Tectonics,* **38**(11), 3975–3989.

Lorenzo-Martín, F., Roth, F. & Wang, R., 2006. Elastic and inelastic triggering of earthquakes in the North Anatolian fault zone, *Tectonophysics,* **424**(3–4), 271–289.

Manga, M., Beresnev, I., Brodsky, E.E., Elkhoury, J.E., Elsworth, D., Ingebritsen, S.E., Mays, D.C. & Wang, C.-Y., 2012. Changes in permeability caused by transient stresses: field observations, experiments, and mechanisms, *Rev. Geophys.,* **50**(2), doi:10.1029/2011RG000382.

Metzger, S. *et al.*, 2017. The 2015 Mw7. 2 Sarez strike-slip Earthquake in the Pamir interior: response to the underthrusting of India's western promontory, *Tectonics,* **36**(11), 2407–2421.

Metzger, S., Ischuk, A., Deng, Z., Ratschbacher, L., Perry, M., Kufner, S.-K., Bendick, R. & Moreno, M., 2020. Dense GNSS profiles across the northwestern tip of the India-Asia collision zone: triggered slip and westward flow of the Peter the First Range, Pamir, into the Tajik depression, *Tectonics,* **39**(2), e2019TC005797, doi:10.1029/2019TC005797.

Michael, A.J., 1984. Determination of stress from slip data: faults and folds, *J. geophys. Res.,* **89**(B13), 11 517–11 526.

Michael, A.J., 1987. Use of focal mechanisms to determine stress: a control study, *J. geophys. Res.,* **92**(B1), 357–368.

Michele, M., Chiaraluce, L., Di Stefano, R. & Waldhauser, F., 2020. Fine-scale structure of the 2016–2017 Central Italy seismic sequence from data recorded at the Italian National Network, *J. geophys. Res.,* **125**(4), e2019JB018440, doi:10.1029/2019JB018440.

Mildon, Z.K., Roberts, G.P., Walker, J. P.F. & Iezzi, F., 2017. Coulomb stress transfer and fault interaction over millennia on non-planar active normal faults: the Mw 6.5–5.0 seismic sequence of 2016–2017, central Italy, *Geophys. J. Int.,* **210**(2), 1206–1218.

Mildon, Z.K., Roberts, G.P., Walker, J.F. & Toda, S., 2019. Coulomb prestress and fault bends are ignored yet vital factors for earthquake triggering and hazard, *Nat. Commun.,* **10**(1), 1–9.

Miller, S.A., 2020. Aftershocks are fluid-driven and decay rates controlled by permeability dynamics, *Nat. Commun.,* **11**(1), doi:10.1038/s41467-020-19590-3.

Miller, S.A. & Nur, A., 2000. Permeability as a toggle switch in fluid-controlled crustal processes, *Earth planet. Sci. Lett.,* **183**(1–2), 133–146.

Morishita, Y., Lazecky, M., Wright, T.J., Weiss, J.R., Elliott, J.R. & Hooper, A., 2020. LiCSBAS: an open-source InSAR time series analysis package integrated with the LiCSAR automated Sentinel-1 InSAR processor, *Remote Sens.,* **12**(3), doi:10.3390/rs12030424.

Nábělek, J. & Xia, G., 1995. Moment-tensor analysis using regional data: application to the 25 March, 1993, Scotts Mills, Oregon, Earthquake, *Geophys. Res. Lett.,* **22**(1), 13–16.

Nalbant, S.S., Steacy, S., Sieh, K., Natawidjaja, D. & McCloskey, J., 2005. Earthquake risk on the Sunda trench, *Nature,* **435**(7043), 756–757.

Nöth, L., 1932. *Geologische Untersuchungen im nordwestlichen Pamirgebiet und mittleren Transalai,* Verlag Dietrich Reimer.

Ogwari, P. & Horton, S., 2016. Numerical model of pore-pressure diffusion associated with the initiation of the 2010–2011 Guy–Greenbrier, Arkansas earthquakes, *Geofluids,* **16**(5), 954–970.

Okada, Y., 1985. Surface deformation due to shear and tensile faults in a half-space, *Bull. seism. Soc. Am.,* **75**(4), 1135–1154.

Parsons, T. & Dreger, D.S., 2000. Static-stress impact of the 1992 Landers earthquake sequence on nucleation and slip at the site of the 1999 m=7.1 Hector Mine earthquake, southern California, *Geophys. Res. Lett.,* **27**(13), 1949–1952.

Peña Castro, A.F., Dougherty, S.L., Harrington, R.M. & Cochran, E.S., 2019. Delayed dynamic triggering of disposal-induced earthquakes observed by a dense array in northern Oklahoma, *J. geophys. Res.,* **124**(4), 3766–3781.

Perfettini, H., Stein, R.S., Simpson, R. & Cocco, M., 1999. Stress transfer by the 1988-1989 Mw = 5.3 and 5.4 Lake Elsman foreshocks to the Loma Prieta fault: unclamping at the site of peak mainshock slip, *J. geophys. Res.,* **104**(B9), 20 169–20 182.

Perry, M., Kakar, N., Ischuk, A., Metzger, S., Bendick, R., Molnar, P. & Mohadjer, S., 2019. Little geodetic evidence for localized Indian subduction in the Pamir-Hindu Kush of Central Asia, *Geophys. Res. Lett.,* **46**(1), 109–118.

Geophysical Survey of the National Academy of sciences of Tajikistan, 2009. International Federation of Digital Seismograph Networks, *Tajikistan National Seismic Network*. https://www.fdsn.org/networks/detail/TJ/, doi:10.7914/SN/TJ.

Pollitz, F.F., Banerjee, P., Bürgmann, R., Hashimoto, M. & Choosakul, N., 2006. Stress changes along the Sunda trench following the 26 December 2004 Sumatra-Andaman and 28 March 2005 Nias earthquakes, *Geophys. Res. Lett.,* **33**(6), doi:10.1029/2005GL024558.

Pozzi, J.-P. & Feinberg, H., 1991. Paleomagnetism in the Tajikistan: continental shortening of European margin in the Pamirs during Indian Eurasian collision, *Earth planet. Sci. Lett.,* **103**(1–4), 365–378.

Qiao, X., Wang, Q., Yang, S., Li, J., Zou, R. & Ding, K., 2015. The 2008 Nura Mw6. 7 earthquake: a shallow rupture on the Main Pamir Thrust revealed by GPS and InSAR, *Geod. Geodyn.,* **6**(2), 91–100.

Rice, J.R. & Cleary, M.P., 1976. Some basic stress diffusion solutions for fluid-saturated elastic porous media with compressible constituents, *Rev. Geophys.,* **14**(2), 227–241.

Robinson, A.C., 2009. Geologic offsets across the northern Karakorum fault: Implications for its role and terrane correlations in the western Himalayan-Tibetan Orogen, *Earth planet. Sci. Lett.,* **279**(1–2), 123–130.

Robinson, A.C., Yin, A., Manning, C.E., Harrison, T.M., Zhang, S.-H. & Wang, X.-F., 2004. Tectonic evolution of the northeastern Pamir: constraints from the northern portion of the Cenozoic Kongur Shan extensional system, western China, *Bull. geol. Soc. Am.,* **116**(7–8), 953–973.

Robinson, A.C., Yin, A., Manning, C.E., Harrison, T.M., Zhang, S.-H. & Wang, X.-F., 2007. Cenozoic evolution of the eastern Pamir: implications for strain-accommodation mechanisms at the western end of the Himalayan-Tibetan Orogen, *Bull. geol. Soc. Am.,* **119**(7–8), 882–896.

Roland, E. & McGuire, J.J., 2009. Earthquake swarms on transform faults, *Geophys. J. Int.,* **178**(3), 1677–1690.

Ross, Z.E., Cochran, E.S., Trugman, D.T. & Smith, J.D., 2020. 3D fault architecture controls the dynamism of earthquake swarms, *Science,* **368**(6497), 1357–1361.

Rutte, D., Ratschbacher, L., Schneider, S., Stübner, K., Stearns, M.A., Gulzar, M.A. & Hacker, B.R., 2017. Building the Pamir-Tibetan Plateau-Crustal stacking, extensional collapse, and lateral extrusion in the Central Pamir: 1. Geometry and kinematics, *Tectonics,* **36**(3), 342–384.

Ryder, I., Bürgmann, R. & Fielding, E., 2012. Static stress interactions in extensional earthquake sequences: an example from the South Lunggar Rift, Tibet, *J. geophys. Res.,* **117**(B9), doi:10.1029/2012JB009365.

Sangha, S., Peltzer, G., Zhang, A., Meng, L., Liang, C., Lundgren, P. & Fielding, E., 2017. Fault geometry of 2015, Mw7. 2 Murghab, Tajikistan earthquake controls rupture propagation: Insights from InSAR and seismological data, *Earth planet. Sci. Lett.,* **462,** 132–141.

Sass, P., Ritter, O., Ratschbacher, L., Tympel, J., Matiukov, V., Rybin, A. & Batalev, V.Y., 2014. Resistivity structure underneath the Pamir and southern Tian Shan, *Geophys. J. Int.,* **198**(1), 564–579.

Schneider, F. *et al.*, 2013. Seismic imaging of subducting continental lower crust beneath the Pamir, *Earth planet. Sci. Lett.,* **375,** 101–112.

Schurr, B., Ratschbacher, L., Sippl, C., Gloaguen, R., Yuan, X. & Mechie, J., 2014. Seismotectonics of the Pamir, *Tectonics,* **33**(8), 1501–1518.

Schurr, B., Moreno, M., Tréhu, A.M., Bedford, J., Kummerow, J., Li, S. & Oncken, O., 2020. Forming a Mogi doughnut in the years prior to and immediately before the 2014 M8.1 Iquique, northern Chile, earthquake, *Geophys. Res. Lett.,* **47**(16), e2020GL088351, doi:10.1029/2020GL088351.

SEISDMC, 2021. Data management centre of the China National Seismic Network at the Institute of Geophysics [Data set], China Earthquake Administration, International Federation of Digital Seismograph Networks. https://doi.org/10.7914/SN/CB.

Shapiro, S.A., Huenges, E. & Borm, G., 1997. Estimating the crust permeability from fluid-injection-induced seismic emission at the KTB site, *Geophys. J. Int.,* **131**(2), F15–F18.

Shapiro, S.A., Patzig, R., Rothert, E. & Rindschwentner, J., 2003. Triggering of seismicity by pore-pressure perturbations: Permeability-related signatures of the phenomenon, in *Thermo-Hydro-Mechanical Coupling in Fractured Rock,* pp. 1051–1066, Birkhäuser Basel.

Shimojo, K., Enescu, B., Yagi, Y. & Takeda, T., 2021. Nucleation process of the 2011 northern Nagano earthquake from nearby seismic observations, *Sci. Rep.,* **11**(1), 1–10.

Sibson, R., 1992. Implications of fault-valve behaviour for rupture nucleation and recurrence, *Tectonophysics,* **211**(1–4), 283–293.

Sippl, C. *et al.*, 2013a. Deep burial of Asian continental crust beneath the Pamir imaged with local earthquake tomography, *Earth planet. Sci. Lett.,* **384,** 165–177.

Sippl, C. *et al.*, 2013b. Geometry of the Pamir-Hindu Kush intermediate-depth earthquake zone from local seismic data, *J. geophys. Res.,* **118**(4), 1438–1457.

Sippl, C., Ratschbacher, L., Schurr, B., Krumbiegel, C., Rui, H., Pingren, L. & Abdybachaev, U., 2014. The 2008 Nura earthquake sequence at the Pamir-Tian Shan collision zone, southern Kyrgyzstan, *Tectonics,* **33**(12), 2382–2399.

Sobel, E.R., Schoenbohm, L.M., Chen, J., Thiede, R., Stockli, D.F., Sudo, M. & Strecker, M.R., 2011. Late Miocene–Pliocene deceleration of dextral slip between Pamir and Tarim: implications for Pamir orogenesis, *Earth planet. Sci. Lett.,* **304**(3–4), 369–378.

Stein, R.S., 1999. The role of stress transfer in earthquake occurrence, *Nature,* **402**(6762), 605–609.

Strecker, M., Frisch, W., Hamburger, M., Ratschbacher, L., Semiletkin, S., Zamoruyev, A. & Sturchio, N., 1995. Quaternary deformation in the eastern Pamirs, Tadzhikistan and Kyrgyzstan, *Tectonics,* **14**(5), 1061–1079.

Strom, A., 2014. Sarez Lake problem: ensuring long-term safety, in *Landslide Science for a Safer Geoenvironment,* pp. 633–639, Springer.

Stübner, K., Ratschbacher, L., Rutte, D., Stanek, K., Minaev, V., Wiesinger, M., Gloaguen, R. & members, P.T., 2013. The giant Shakhdara migmatitic gneiss dome, Pamir, India-Asia collision zone: 1. Geometry and kinematics, *Tectonics,* **32**(4), 948–979.

Tanaka, S., Ohtake, M. & Sato, H., 2002. Evidence for tidal triggering of earthquakes as revealed from statistical analysis of global data, *J. geophys. Res.,* **107**(B10), ESE 1–1-ESE 1-11.

Teshebaeva, K., Sudhaus, H., Echtler, H., Schurr, B. & Roessner, S., 2014. Strain partitioning at the eastern Pamir-Alai revealed through SAR data analysis of the 2008 Nura earthquake, *Geophys. J. Int.,* **198**(2), 760–774.

Thiede, R.C., Sobel, E.R., Chen, J., Schoenbohm, L.M., Stockli, D.F., Sudo, M. & Strecker, M.R., 2013. Late Cenozoic extension and crustal doming in the India-Eurasia collision zone: new thermochronologic constraints from the NE Chinese Pamir, *Tectonics,* **32**(3), 763–779.

Thomas, J.-C., Chauvin, A., Gapais, D., Bazhenov, M., Perroud, H., Cobbold, P. & Burtman, V., 1994. Paleomagnetic evidence for Cenozoic block rotations in the Tadjik depression (Central Asia), *J. geophys. Res.,* **99**(B8), 15 141–15 160.

Thurber, C.H., 1983. Earthquake locations and three-dimensional crustal structure in the Coyote Lake area, central California, *J. geophys. Res.,* **88**(B10), 8226–8236.

Toda, S. & Stein, R.S., 2020. Long-and short-term stress interaction of the 2019 Ridgecrest sequence and Coulomb-based earthquake forecasts, *Bull. seism. Soc. Am.,* **110**(4), 1765–1780.

Toda, S., Stein, R.S., Reasenberg, P.A., Dieterich, J.H. & Yoshida, A., 1998. Stress transferred by the 1995 Mw=6.9 Kobe, Japan, shock: effect on aftershocks and future earthquake probabilities, *J. geophys. Res.,* **103**(B10), 24 543–24 565.

Utsu, T., Ogata, Y. *et al.*, 1995. The centenary of the Omori formula for a decay law of aftershock activity, *J. Phys. Earth,* **43**(1), 1–33.

Valoroso, L., Chiaraluce, L., Piccinini, D., Di Stefano, R., Schaff, D. & Waldhauser, F., 2013. Radiography of a normal fault system by 64,000 high-precision earthquake locations: The 2009 L'Aquila (central Italy) case study, *J. geophys. Res.,* **118**(3), 1156–1176.

Waldhauser, F. & Ellsworth, W.L., 2000. A double-difference earthquake location algorithm: method and application to the northern Hayward fault, California, *Bull. seism. Soc. Am.,* **90**(6), 1353–1368.

Wang, R., Lorenzo-Martin, F. & Roth, F., 2006. PSGRN/PSCMP—a new code for calculating co- and post-seismic deformation, geoid and gravity changes based on the viscoelastic-gravitational dislocation theory, *Comput. Geosci.,* **32**(4), 527–541.

Wells, D.L. & Coppersmith, K.J., 1994. New empirical relationships among magnitude, rupture length, rupture width, rupture area, and surface displacement, *Bull. seism. Soc. Am.,* **84**(4), 974–1002.

Wessel, P., Smith, W.H., Scharroo, R., Luis, J. & Wobbe, F., 2013. Generic mapping tools: improved version released, *EOS, Trans. Am. geophys. Un.,* **94**(45), 409–410.

Wiseman, K. & Burgmann, R., 2011. Stress and seismicity changes on the Sunda megathrust preceding the 2007 Mw 8.4 earthquake, *Bull. seism. Soc. Am.,* **101**(1), 313–326.

Woessner, J. & Wiemer, S., 2005. Assessing the quality of earthquake catalogues: estimating the magnitude of completeness and its uncertainty, *Bull. seism. Soc. Am.,* **95**(2), 684–698.

Woo, J.-U., Kim, M., Sheen, D.-H., Kang, T.-S., Rhie, J., Grigoli, F., Ellsworth, W.L. & Giardini, D., 2019. An in-depth seismological analysis revealing a causal link between the 2017 M_W5.5 pohang earthquake and EGS project, *J. geophys. Res.,* **124**(12), 13 060–13 078.

Worthington, J.R. *et al.*, 2020. The Alichur dome, South Pamir, western India–Asia collisional zone: detailing the Neogene Shakhdara–Alichur syn-collisional gneiss-dome complex and connection to lithospheric processes, *Tectonics,* **39**(1), e2019TC005735, doi:10.1029/2019TC005735.

Yadav, R., Gahalaut, V., Chopra, S. & Shan, B., 2012. Tectonic implications and seismicity triggering during the 2008 Baluchistan, Pakistan earthquake sequence, *J. Asian Earth Sci.,* **45,** 167–178.

Yu, C., Li, Z., Penna, N.T. & Crippa, P., 2018. Generic atmospheric correction model for Interferometric Synthetic Aperture Radar observations, *J. geophys. Res.,* **123**(10), 9202–9222.

Yuan, X., Schurr, B., Bloch, W., Xu, Q. & Zhao, J., 2018a. East Pamir Network. GFZ Data Services. doi:10.14470/3U7560589977.

Yuan, X., Schurr, B., Kufner, S.-K. & Bloch, W., 2018b. Sarez Pamir aftershock seismic network. GFZ Data Services , doi:10.14470/4U7561589984.

Yushin, I., Sass, M., Karapetov, S., Altukhov, S., Teplov, I., Raeakov, C., Harkov, S. & Davidchenko, A., 1964. *1: 200,000 maps of the Tajik SSR,* Russian Geological Research Institute, Nedra, Moscow.

Zhou, Y., He, J., Oimahmadov, I., Gadoev, M., Pan, Z., Wang, W., Abdulov, S. & Rajabov, N., 2016. Present-day crustal motion around the Pamir Plateau from GPS measurements, *Gondwana Res.,* **35,** 144–154.

Ziv, A. & Rubin, A.M., 2000. Static stress transfer and earthquake triggering: No lower threshold in sight?, *J. geophys. Res.,* **105**(B6), 13 631–13 642.

Zubovich, A., Metzger, S., Schöne, T., Kley, J., Mosienko, O., Zech, C., Moldobekov, B. & Shsarshebaev, A., 2022. Cyclic fault slip under the magnifier: Co- and postseismic response of the Pamir front to the 2015 Mw 7.2 Sarez, Central Pamir, earthquake, *Tectonics,* **41**(9), e2022TC007213, doi:10.1029/2022TC007213.

Zubovich, A.V. *et al.*, 2010. GPS velocity field for the Tien Shan and surrounding regions, *Tectonics,* **29**(6), doi:10.1029/2010TC002772.

Zubovich, A.V., Schöne, T., Metzger, S., Mosienko, O., Mukhamediev, S., Sharshebaev, A. & Zech, C., 2016. Tectonic interaction between the Pamir and Tien Shan observed by GPS, *Tectonics,* **35**(2), 283–292.

SUPPORTING INFORMATION

Supplementary data are available at *GJI* online.

Figure S1. Comparison of event locations for the Sarez earthquake (Fig. 4 of the main text) after the different steps of the event location. Centre panel: map view. Right panel: across-strike profile. Lower panel: along-strike profile. Grey dots are hypocentres which could only be located with *simulps*, but not relocated. Black dots are hypocentres before and red dots after the re-location with *hypoDD*.
Figure S2. As Fig. S1, but for the Sary-Tash earthquake (Fig. 6 of the main text).
Figure S3. As Fig. S1, but for the Muji earthquake (Fig. 7 of the main text).
Figure S4. Subsurface model (Sippl *et al*. 2013b) used for the determination of regional moment tensors.
Figure S5. Moment magnitudes of seismic events. Comparison of regional moment tensors (a) and magnitudes (b) with results by NEIC. (wr) regional (ww) W-phase. (c) Calibration of local magnitudes with parameters of eq. (1) of the main text. (d) Magnitude distribution of the entire catalogue. Completeness magnitude M_c, and most frequent magnitude M_c^{min}.
Figure S6. Results of moment tensor inversion for event 8 (Fig. S5), with observed (black) and modelled (red) waveforms for vertical (Z), radial (R) and transverse (T) component on the stations named on the left. Event backazimuth and distance given below station name.
Figure S7. As Fig. S6, but for event 11 (Fig. S5).
Figure S8. Spatio-temporal evolution of seismicity along the (top panel) southern continuation of the SKFS; (middle panel) northern continuation of the SKFS; (bottom panel) continuation of the MPTS into the Muji fault. v is propagation velocity $r = vt$. D according to eq. (8) of the main text.
Figure S9. Aftershock characteristics of main shock vicinities A, B, C, E, G and I. Left-hand column: cumulative aftershocks after the main shock (A shown before and after installation of 8H network) and parameters of modified Omori's Law (Utsu *et al*. 1995). Middle column: aftershock rate over time. Right-hand column: deviation of aftershock rate from Omori's law over time. Even though time intervals of increased aftershock activity exist, they to not correlate with each other in between earthquake sequences.

Figure S10. Time succession of seismicity within the Northwest Pamir Earthquake Swarm *D*, colour-coded by time after the onset of the intense activity on 4 August 2016. Top panel: map-view. Bottom panel: Along-strike view. Bottom: Across-strike view. A possible earthquake migration pattern is not apparent from the data.
Figure S11. Perpendicular baseline (B_{perp}) against time for InSAR frame 100A 052 (Figs 4 and S13). Lines indicate combination of acquired images to compute differential interferograms.
Figure S12. As Fig. S11, but for frame 005D 050.
Figure S13. InSAR time-series as in Fig. 5 of the main text. Left-hand panel: rate map before conversion to displacement. Right-hand panel: nominal uncertainty of displacement rate.
Figure S14. Contributions of distinct stress sources to the change in Coulomb failure stress (ΔCFS) on the fault plane of the Sary-Tash earthquake in dependence of friction (μ) and Skempton's parameter (β) under constant apparent friction ($\mu^{'}$).
Figure S15. As Fig. S14, but for the Muji earthquake.
Figure S16. Sensitivity analysis of Coulomb failure stress changes at the Sary-Tash hypocentre C^* due to the Sarez earthquake, post-seismic slip on the Sarez fault and foreshock $e^{'}$. Contributions (from left to right) of normal distributed variations around the preferred values (stars) of receiver fault's strike, dip and rake (with a standard deviation of 5°), Lamés parameters λ and G (standard deviation of 5 GPa), friction coefficient μ, and Skempton's parameter β (standard deviation 0.2, ensuring [0, 1] range). Resulting median, 5 and 95 per cent quantiles under the assumption of input uncertainties.
Figure S17. Sensitivity analysis of Coulomb failure stress changes as in Fig. S16, but due to the Sarez and Sary-Tash earthquakes at the Muji main shock E^* or Muji foreshock $e^{'}$ hypocentre, both of which yield the same results within 100 Pa.
Figure S18. Fault orientation relative to the ambient stress field (eq. 5 of the main text) against Omori-Utsu p-value (Fig. S9; eq. 4). Orientation is parametrized as the dot product (i.e. cosine of the angle) between the fault plane normal vector (Table 1) and σ_1 (eq. 5). We regard the p-value of sequence I as an overestimate, because it occurred while the seismic network was dismantled. The recorded aftershock sequence is therefore likely incomplete. A weak trend suggests a faster aftershock decay when the fault is more closely oriented perpendicular to σ_1.